UNIVERSIÄT DUISBURG-ESSEN

Dynamic Unidirectional Anisotropy in FeGe studied by Ferromagnetic Resonance

Masterarbeit zur Erlangung des akademischen Grades

MASTER OF SCIENCE (M.SC.)

vorgelegt von

Nicolas Mathias Josten

aus Essen

Fakultät für Physik der Universität Duisburg-Essen

Arbeitsgruppe von Prof. Dr. Michael Farle

Zusammenfassung

Polykristallines B20 FeGe, das sich durch die ihm innewohnende Dzyaloshinskii-Moriya Wechselwirkung auszeichnet, wurde mittels ferromagnetischer Resonanz Experimente untersucht. Die Messungen zeigen eine unidirektionale Anisotropie, das heißt, dass sich das Resonanzfeld bei Inversion des Magnetfeldes verschiebt. Magnetostatische Messungen zeigen diese Anisotropie nicht, es handelt sich also um einen dynamischen Effekt. In dieser Arbeit werden zwei Modelle beschrieben, um eine solche ferromagnetische Resonanz Messung auszuwerten. Das erste fügt der freien Energiedichte einen zusätzlichen unidirektionalen Anisotropieterm hinzu, der wie eine Kristallanisotropie wirkt, aber rein phenomenologischer Natur ist. Das zweite nimmt einen Temperaturunterschied zwischen den beiden Feldrichtungen an, der sich in einer Änderung der Magnetisierung und somit auch einer Änderung der Formanisotropie niederschlägt. Dieser Temperaturunterschied ΔT kann temperaturabhängig ausgewertet werden und beträgt maximal $7.1\,\mathrm{K} \pm 0.8\,\mathrm{K}$ bei $T = 200\,\mathrm{K}$. Um diesen Temperaturunterschied zu erklären wurde ein Modell basierend auf Magnonenstreuung entwickelt. Durch die asymmetrische Dispersionsrelation, hervorgerufen von der Dzyaloshinskii-Moriya Wechselwirkung, folgt eine Änderung der Magnonenstreuung je nach Feldrichtung. Dies führt zu einer Änderung der Temperatur des Magnonensystems und somit zur unidirektionalen Anisotropie.

Abstract

Polycrystalline B20 FeGe, which is characterized by its inherent Dzyaloshinskii-Moriya interaction, was investigated by ferromagnetic resonance experiments. The measurements display a unidirectional anisotropy, meaning that an inversion of the magnetic field changes the resonance field. Magnetostatic measurements do not show this anisotropy, thus it is a dynamic effect. In this work, two models are described to analyse such ferromagnetic resonance measurements. The first one introduces an additional term to the free energy density with unidirectional symmetry, which acts like a magnetocrystalline anisotropy. This term is purely phenomenological. The second method is based on a temperature change inside the sample after magnetic field inversion. This results in a change of the magnetization and thus also in a change of shape anisotropy. This temperature change ΔT can be evaluated as a function of the temperature and is at its maximum $7.1\,\mathrm{K} \pm 0.8\,\mathrm{K}$ at $T = 200\,\mathrm{K}$. To justify such a temperature change a magnon scattering model was developed. It is based on asymmetric magnon scattering, caused by the asymmetric magnon dispersion in systems with Dzyaloshinskii-Moriya interaction. This leads to an inhomogeneous change of the temperature in the magnonic system and thus to the observed unidirectional anisotropy.

Publications

- N. Josten, T. Feggeler, R. Meckenstock, D. Spoddig, M. Spasova, K. Chai, I. Radulov, Z.-A. Li, O. Gutfleisch, M. Farle, and B. Zingsem, "Dynamic unidirectional anisotropy in cubic FeGe with antisymmetric spin-spin-coupling." *Sci Rep* 10, 2861 (2020). https://doi.org/10.1038/s41598-020-59208-8

Contents

Page

List of Abbreviations

1. Introduction and Motivation **1**

2. Theoretical Background **3**
2.1. Magnetization and Free Energy Density . . . 3
2.2. Magnetic Energy Contributions . . . 4
2.2.1. Symmetric and Asymmetric Exchange Interaction . . . 4
2.2.2. Zeeman Term and Demagnetization . . . 5
2.2.3. Magnetocrystalline Anisotropy . . . 5
2.3. Ferromagnetic Resonance . . . 6
2.3.1. Ferromagnetic Resonance Lineshape . . . 7
2.3.2. Calculation of the Resonance Position . . . 7
2.3.3. Ferromagnetic Resonance Linewidth . . . 7
2.4. Chirality . . . 9

3. Sample Characteristics **10**
3.1. Crystallography of Cubic FeGe . . . 10
3.2. Magnetic Properties of B20 FeGe . . . 12
3.3. Sample Preparation . . . 14
3.4. X-ray Diffraction Measurements . . . 14

4. Dynamic Unidirectional Anisotropy **17**
4.1. Angular Dependent Ferromagnetic Resonance . . . 17
4.2. Vibrating Sample Magnetometry . . . 22
4.3. Temperature Dependent Ferromagnetic Resonance . . . 26
4.3.1. Introduction of a Magnetization-Dependent Temperature Model . . . 30
4.4. Adapted Unidirectional Anisotropy Model . . . 32
4.5. Ferromagnetic Resonance Lineshape . . . 34
4.5.1. Description of the FeGe Lineshape . . . 34
4.5.2. Modeling the Ferromagnetic Resonance Spectra of a Polycrystal . . . 40

5. Magnon-Scattering Model for FeGe **43**
5.1. Dispersion Relation with and without DMI . . . 43
5.2. Heat Capacity of Magnons in FeGe . . . 45
5.3. Geometry Dependent Heating by Magnon-Scattering . . . 47
5.3.1. Limits of the Heating Model . . . 50

6. Discussion and Outlook **51**

A. Appendix **53**

A.1. Ferromagnetic Resonance Spectra of the "Cylindrical" Sample 53

A.2. Dependence of $\tilde{T}$ on the magnetization angles 53

A.3. Modeling of Polycrystals 54

A.3.1. Evenly Distributed Points on a Unitsphere 54

A.3.2. Free Energy Density in Consideration of Rotation Matrices 56

References **58**

List of Abbreviations

DMI Dzyaloshinskii–Moriya interaction 1

FMR ferromagnetic resonance 1

XRD X-ray diffraction 15

VSM vibrating sample magnetometry 22

PID proportional–integral–derivative controller 18

oop out-of-plane 18

ip in-plane 18

MAE magnetic anisotropy energy density 23

PDF probability density function 54

CDF cumulative distribution function 55

1 Introduction and Motivation

Dzyaloshinskii–Moriya interaction (DMI) was introduced to the theory of magnetism to explain weak ferromagnetism in otherwise antiferromagnetic samples [1, 2]. One necessity for the occurence of DMI is a broken inversion symmetry. This broken inversion symmetry can either be manufactured, for example through interfaces in thin-films, which is then called interfacial DMI [3, 4], or is an inherent property of the crystal lattice like in the B20 crystals MnSi or FeGe [5–8]. DMI favors a perpendicular alignment of neighboring spins and therefore competes with exchange interaction, resulting in chiral spin textures like helices [7] and skyrmions [9, 10]. Skyrmions are topologically stable magnetic vortices and are promising for applications in spintronics, e.g. as racetrack memories [11] and spin logic devices [12].
DMI not only influences the magnetostatic but also the magnetodynamic properties by introducing an additional term to the spin-wave dispersion proportional to the wavenumber [13, 14]. This leads to non-reciprocal spin-waves, meaning that spin-waves traveling with the same frequency in opposite directions have different wavelengths. It has been predicted, that these spin-waves form complex standing modes in confined geometry [15]. Polycrystalline FeGe was investigated in my bachelor thesis [16] with the motive to measure these standing spin-wave modes. For that, micron sized FeGe samples were cut and placed inside an R-type microresonator [17–19] for ferromagnetic resonance (FMR) [20–22] measurements. In the obtained spectra, a multitude of resonances were visible and ultimately attributed to an inclined surface simultaneously satisfying a collection of boundary conditions for standing spin-waves. Surprisingly, all results pointed to the conclusion that a unidirectional anisotropy, observed as a shift of the resonance position after magnetic field inversion, had to be present. It was presumed that even though the non-reciprocity creates complex standing modes, these modes should still be inversion symmetric. A comparison with older FMR data measured by Thomas Feggeler [23] on bulk FeGe samples inside a conventional cavity revealed, that even the uniform mode displayed this kind of anisotropy. Unidirectional anisotropy is not unheard of in FMR measurements. For example, it can occur in systems with exchange bias [24], which has never been reported for FeGe.
In this work, the unidirectional anisotropy is investigated for both angular and temperature dependence. The relevant theoretical background is given in Ch. 2. First the Helmholtz free energy density [25] [21, p. 31f.] is introduced, whereby all important magnetic contributions appearing in this work are presented. The theory of FMR is discussed with regards to the resonance position, lineshape and linewidth. Finally a section is dedicated to chirality [26], which is an important aspect of the FeGe crystal lattice. Chapter 3 is devoted to the preparation and properties of FeGe [27, 28]. Among other things, the known magnetic properties of FeGe are brought together from literature. In Ch. 4, angular and temperature dependent FMR measurements are presented, particularly with regard to the unidirectional anisotropy. A phenomenological model for the free energy density is introduced to quantify

the strength of the unidirectional anisotropy. The absence of any asymmetry in the hysteresis of FeGe points to its dynamic nature. Temperature dependent FMR measurements lead to the conclusion that this effect can also be described through a temperature difference between opposite magnetic field directions. Therefore, a second model for the free energy density is proposed, which takes this temperature difference into consideration. It is able to fit to the data better than the already mentioned phenomenological model. After this, different contributions to the FMR linewidth are discussed with the largest one identified as an inhomogeneous demagnetization field inside the irregularly shaped sample. Chapter 5 gives a theoretical model to explain the assumed temperature difference between opposite field directions during dynamic excitation. It is based on asymmetric magnon scattering due to the non-reciprocity of spin-waves in DMI systems [13]. Furthermore, the energy needed for such a temperature change is calculated based on the heat capacity of magnons in FeGe and is found to lie below the energy provided by the microwave. In Ch. 6, the results of this work are discussed and a summary is given on unanswered questions concerning the unidirectional anisotropy.

The calculations and plots in this thesis were done with Wolfram Mathematica 12.0 Student Edition. Further editing of these plots and the illustrations were made with Corel DRAW 2017. This thesis was written with LaTeX.

2 Theoretical Background

This chapter centers on the theory of magnetism relevant for this work. Especially FMR is discussed in detail. For an overview of ferromagnetism in general see the book of Aharoni [29]. For a basic understanding of FMR, the books of Vonsovskii [20] and Gurevich and Melkov [21] are well suited.

2.1 Magnetization and Free Energy Density

The magnetic moment $\vec{\mu}$ of any material is given by the torque $\vec{I}$ it experiences inside a magnetic field $\vec{B}$ and is defined by

$$\vec{I} = \vec{\mu} \times \vec{B}. \tag{2.1}$$

Such a magnetic moment can either be an intrinsic property of the material, or it can be induced by an external magnetic field or an electrical current. The magnetization $\vec{M}$ is the magnetic moment per volume [29, p. 1] or, in other words, the magnetic moment density. Due to sample sizes far above atomic length scales all interpretations and calculations can be performed with methods and concepts of statistical physics. One of these concepts is the Helmholtz free energy [25] [21, p. 31f.], which is the difference between the inner energy U and the product of temperature T and entropy S. The free energy density F [30, p. 196] is the Helmholtz free energy per volume V and is therefore defined as

$$F = \frac{U - TS}{V}. \tag{2.2}$$

The free energy density in this work refers to the magnetic part of the free energy density. The thermodynamic equilibrium position of the magnetization minimizes the free energy density [22, p. 779]. The absolute value and direction of the effective magnetic field can be determined through

$$\vec{B}_{\text{eff}} = -\frac{\delta F}{\delta \vec{M}} = -\frac{\partial F}{\partial \vec{M}} + \sum_{i=1}^{3} \frac{\partial}{\partial x_i} \left(\frac{\partial F}{\partial \left(\partial \vec{M} / \partial x_i \right)} \right). \tag{2.3}$$

Here δ denotes the functional derivative [25,31] [21, p. 33]. In the case of thermal equilibrium it is also parallel to the magnetization [20, p. 21]. Due to Eq. 2.3, all contributions to the magnetic free energy can be treated as magnetic fields acting on the sample. These fields are often fictitious. The molecular field postulated to treat ferromagnetism in classical electrodynamics is a prominent example for a fictitious field [32]. It is explained by the exchange interaction introduced in the next section.

2.2 Magnetic Energy Contributions

2.2.1 Symmetric and Asymmetric Exchange Interaction

The Heisenberg model [33] is devised to explain ferromagnetism and is based on the assumption of having localized electrons around atoms inside a crystal lattice. Since electrons are fermions with spin 1/2, they are subject to the Pauli exclusion principle [34] favoring parallel or antiparallel spin alignment. Simultaneously, electrons carry a negative charge and thus feel a repulsive Coulomb force from one another. These together create an electron-electron interaction called exchange interaction [35, p. 459ff.], which is a purely quantum mechanical effect. Since the electron wave functions have to overlap, it is only a nearest-neighbor interaction. The exchange interaction is not limited to ferromagnetism but can also be used to explain antiferromagnetism [36] or the paramagnetism of oxygen [37]. DMI [1, 2] is another type of nearest-neighbor interaction favoring the perpendicular alignment of spins and can only exist in a system with broken inversion symmetry. If this broken inversion symmetry is an intrinsic property of the crystal structure, one refers to it as bulk DMI. It can be explained through spin-orbit coupling [2]. The combined Hamiltonian of exchange interaction and DMI can be written as

$$\hat{H} = \hat{H}_{\mathrm{EX}} + \hat{H}_{\mathrm{DMI}} = -\frac{1}{2}\sum_{i\neq j}\frac{J_{ij}^{A}}{2}\vec{s}_i \cdot \vec{s}_j + \frac{1}{2}\sum_{i\neq j}\vec{D}_{ij}\cdot(\vec{s}_i \times \vec{s}_j). \tag{2.4}$$

Here $\vec{s}_i$ and $\vec{s}_j$ are the spin momenta on the lattice sites i and j respectively, J_{ij}^{A} the exchange constant, and $\vec{D}_{ij}$ the DMI-vector between them. DMI is often denoted as asymmetric exchange, since the exchange interaction and DMI can be combined to one joint exchange tensor with the DMI-vector components being the non-diagonal entries. The connection between broken inversion symmetry and DMI can be seen in Eq. 2.4, since an inversion of the spin momenta in the cross product also yields an inversion of the sign breaking the inversion symmetry. The non-uniform free energy density contribution of the exchange interaction and bulk DMI can be written as

$$\mathrm{F}_{\mathrm{EX}} + \mathrm{F}_{\mathrm{DMI}} = \frac{A}{2M^2}\left(\nabla\vec{M}\right)^2 + \frac{d}{M^2}\vec{M}\cdot\left(\nabla\times\vec{M}\right). \tag{2.5}$$

A is the exchange stiffness and d the DMI constant [7,13] [21, p. 179]. The coupled magnetic moments in a ferromagnet form through Eq. 2.4 an oscillatory system, which can carry dynamic oscillations [21, p. 179ff.] [20, p. 78ff.]. These oscillations are called spin-waves in a semi-classical approach and magnons as quasi particles in a quantum mechanical model. A further description of spin-waves and their dispersion follows in Ch. 5.

2.2.2 Zeeman Term and Demagnetization

The Zeeman effect [38] describes the energy contribution of a static external magnetic field on the magnetization. It is a shift of the energy favoring a parallel alignment. The free energy density contribution of the Zeeman effect $\mathrm{F_Z}$ can be written as

$$\mathrm{F_Z} = -\vec{M} \cdot \vec{B}_{\mathrm{ext}}. \tag{2.6}$$

$\mathrm{F_Z}$ is the scalar projection of the magnetization $\vec{M}$ on the external magnetic field $\vec{B}_{\mathrm{ext}}$ [21, p. 34]. An additional demagnetization field has to be considered in a sample with finite dimensions. The demagnetization field $\vec{B}_{\mathrm{dem}}$ can be determined using the matrix multiplication of the demagnetization tensor $\boldsymbol{N}$ with the magnetization [21, p. 23], so that

$$\vec{B}_{\mathrm{dem}} = -\mu_0 \boldsymbol{N} \vec{M}. \tag{2.7}$$

The free energy density contribution of the demagnetization field [21, p. 34] is then

$$\mathrm{F_{dem}} = \frac{\mu_0}{2} \vec{M} \boldsymbol{N} \vec{M}. \tag{2.8}$$

It is often referred to as the shape anisotropy. When the sample shape is not an ellipsoid, the demagnetization field inside the sample is not uniform [29, p. 130] and can, depending on the specific problem, be calculated analytically [39] or through simulation [40]. However, most simple geometric bodies can be approximated as an equivalent ellipsoid [41].

2.2.3 Magnetocrystalline Anisotropy

Although we use a semi-classical model of magnetism one has to be aware of the underlying atomic structure. Ordinary matter can exist in the form of ordered crystals that impose certain symmetry conditions on the magnetism of the material. This is known as magnetocrystalline anisotropy [29, p. 84] [21, p. 37ff.] and gives rise to preferred magnetization directions. It is expressed as additional terms in the free energy density. Calculations of these terms may need the usage of phenomenological power series expansions containing the correct symmetry [29, p. 85]. The anisotropy constants have to be measured. An example for the cubic crystal anisotropy will be given in Sec. 3.2.

2.3 Ferromagnetic Resonance

To describe the dynamic behavior of the magnetization inside an effective magnetic field the Landau-Lifshitz-Gilbert equation, written as

$$\frac{\partial \vec{M}}{\partial t} = \gamma \vec{M} \times \vec{B}_{\text{eff}} - \frac{\alpha}{M} \vec{M} \times \frac{\partial \vec{M}}{\partial t}, \tag{2.9}$$

is used [42, 43]. The first term of the differential equation describes a precession of the magnetization around the effective magnetic field, while the second accounts for energy dissipation. α is the damping parameter. To solve the equation, an Ansatz is needed [44] [21, p. 10ff.]. First, a constant magnetization $\vec{M}_0$ and an effective field $\vec{B}_0$ pointing in the same direction (w.l.o.g. this can be the z-axis of a Cartesian coordinate system) are assumed. Additionally, their small oscillating perpendicular pertubations $\vec{b}$ and $\vec{m}$ are considered with a phase shift of $\pi/2$ between them, so that

$$\begin{aligned} \vec{B} &= \vec{B}_0 + \vec{b} = \vec{B}_0 + \vec{b}_0 \mathrm{e}^{i\left(\omega t + \frac{\pi}{2}\right)} \\ \text{and} \quad \vec{M} &= \vec{M}_0 + \vec{m} = \vec{M}_0 + \vec{m}_0 \mathrm{e}^{i\omega t}. \end{aligned} \tag{2.10}$$

For example, $\vec{b}$ can be the magnetic field component of a microwave. The solution links the dynamic oscillation of the magnetization $\vec{m}$ with that of the magnetic field $\vec{b}$ through the high-frequency magnetic susceptibility tensor $\boldsymbol{\chi}$, so that

$$\vec{m} = \boldsymbol{\chi} \vec{b}. \tag{2.11}$$

This means that the sample absorbs power from the oscillating magnetic field. In a cavity based FMR experiment, where a sample is excited through a microwave, the measured signal is proportional to the density P of the absorbed power. When calculated [45, 46] [22, p. 767], it has the form

$$P = \frac{1}{2} \omega \mu_0 \left(\frac{b_0}{\mu_0 \mu_r} \right)^2 \operatorname{Im}\left(\chi_{11}\right). \tag{2.12}$$

It is important to note that the dependence on the imaginary part of the first tensor component of the high frequency susceptibility tensor stems from certain assumptions on the coordinate system and the field and magnetization directions in Eq. 2.10. A general treatment can be found in [47]. In such a general treatment χ'' denotes the imaginary part of the respective tensor component contributing to the measured FMR-signal. The field (or frequency) with the highest absorption is the FMR position. In the case of $\alpha = 0$, the absorption diverges at the resonance position.

2.3.1 Ferromagnetic Resonance Lineshape

The power density shown in Eq. 2.12 has a Lorentzian-shape [21, p. 20], which can be written as

$$L = \frac{a\Delta x}{\Delta x^2 + (x - x_0)^2}. \tag{2.13}$$

Here $a/\Delta x$ is the maximum amplitude, Δx is the half width at half maximum, and x_0 is the resonance position. In a typical FMR experiment, the microwave frequency is kept constant, while the magnetic field is varied. Then, x_0 corresponds to a resonance field. This method of calculation assumes perfect sample conditions. Other effects like the penetration depth of the microwaves are not considered and lead to an asymmetric lineshape also denoted as a Dysonian lineshape [48]. This is written as

$$D = \frac{a\left(\Delta x + \beta\left(x - x_0\right)\right)}{\Delta x^2 + (x - x_0)^2}. \tag{2.14}$$

β is an additional asymmetry parameter. This asymmetry shifts the maximum amplitude of the curve away from the resonance position x_0, as can be seen in Fig. 2.1.

2.3.2 Calculation of the Resonance Position

From Eq. 2.3, it follows that the absolute value of the effective magnetic field can be determined using the free energy density. Solving Eq. 2.9 by approximating the free energy density with a Taylor series about the equilibrium position of the magnetization, one obtains

$$\omega = \frac{\gamma\sqrt{1+\alpha^2}}{M\sin\left(\theta\right)}\sqrt{\frac{\partial^2}{\partial\theta^2}F\frac{\partial^2}{\partial\phi^2}F - \left(\frac{\partial^2}{\partial\theta\partial\phi}F\right)^2} \tag{2.15}$$

for the ferromagnetic resonance frequency [20, p. 67]. This provides a convenient way to analyse FMR data, because a suitable model of the free energy density can reproduce the measured resonance positions. These models consist of combinations of different magnetic energy contributions with some of them introduced in Sec. 2.2.

2.3.3 Ferromagnetic Resonance Linewidth

The linewidth of the resonance curve is defined as the full width at half maximum of the resonance line. In an experimental setup, where the magnetic field is swept at a constant frequency, the linewidth is denoted as ΔB. One mechanism leading to a broadening of the resonance line is the intrinsic magnetic damping. Using Eq. 2.9 the intrinsic linewidth ΔB_{int}

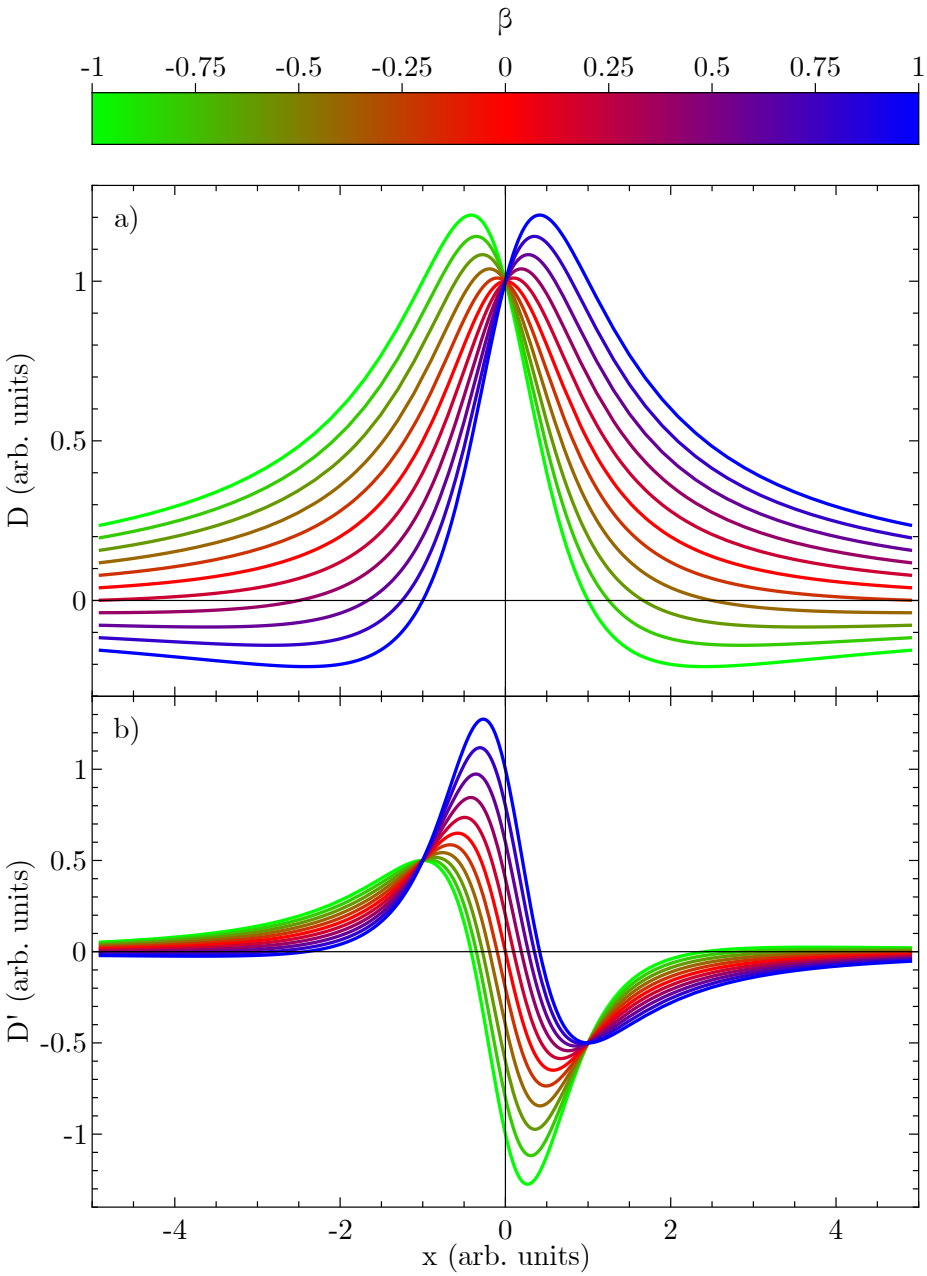

Figure 2.1.: Plot of a Dysonian lineshape. (a) D from Eq. 2.14 and (b) its derivative D' with respect to x. The asymmetry parameter β was varied between 0 and 1, which is color coded above the figure. The parameters used are $x_0 = 0$, $a = 1$, and $\Delta x = 1$. The shift of the maximum amplitude (or the zero crossing in the derivative) away from x_0 with increasing β can be seen.

can be calculated as a function of α and F [49] [20, p. 67] as

$$\Delta B_{\text{int}} = \frac{\partial B_{\text{res}}}{\partial \omega} \frac{\gamma \alpha}{M} \left(\frac{\partial^2 F}{\partial \theta^2} + \frac{1}{\sin(\theta)} \frac{\partial^2 F}{\partial \phi^2} \right). \tag{2.16}$$

According to the reciprocal dependence of M in this equation, without additional anisotropy the intrinsic linewidth near the Curie temperature T_C increases. Until now, only an individual resonance line in a uniform sample was discussed. In a real sample different parts of the sample can lead to different resonance frequencies. This can give a distribution of resonance lines in a measured FMR spectrum resulting in additional contributions to the linewidth. Such a distribution of resonance lines can have different origins with the most important ones in this work being the broadening due to polycristallinity [21, p. 54] [50,51] and due to an inhomogeneous field distribution inside the sample.

2.4 Chirality

Chirality is the inability of a geometric object to coincide with its own mirror image. The term was coined by lord Kelvin [52] more than one hundred years ago. The reflection of a mirror image is again the original image. Therefore, chiral objects always come in the form of two related manifestations, which are called enantiomers. Some three dimensional chiral objects like helices can be described by their handedness, which is their helicity and can be either right-handed or left-handed. Symmetry operations can thus be classified by preservation of the handedness as symmetry operations of the first (preserving) and second (not preserving) kind [26]. Since rotation is a symmetry operation of the first kind, chiral objects keep their chiral properties even inside a polycrystalline sample or when dissolved in a solvent.

This is, for example, used in circular dichroism measurements [53] to analyse the structure of chiral molecules, taking advantage of the different absorption of right and left circular polarized light by the enantiomers. In this work, the magnetic interactions arising from the chirality of FeGe is investigated. Investigations on the chirality itself can be found in [54,55]. A basic description of the origin of chirality in FeGe is given in the following chapter.

3 Sample Characteristics

3.1 Crystallography of Cubic FeGe

Similar to the general summary of the B20 structure given in [56, p. 33f.], here, particularly the B20 crystal FeGe denoted as cubic FeGe is explained. It was first described by Richardson [27, 28] in 1967. FeGe has a cubic crystal symmetry with the space group $P2_13$ and a lattice parameter of $a = 4.700\,\text{Å} \pm 0.002\,\text{Å}$. The density is $\varrho = 8.22\,\text{g}\,\text{cm}^{-3}$. The following Wyckoff positions [57] are occupied, where u is $u_{Fe} = 0.1352$ or $u_{Ge} = 0.8414$ depending on the respective element [28]:

$$4(a) \qquad (u,u,u) \qquad (-u,\tfrac{1}{2}+u,\tfrac{1}{2}-u) \qquad (\tfrac{1}{2}-u,-u,\tfrac{1}{2}+u) \qquad (\tfrac{1}{2}+u,\tfrac{1}{2}-u,-u)$$

This means the unit cell consists of 4 atoms of each type. Due to its chiral properties the crystal structure comes in the form of two enantiomers depicted in Fig. 3.1. The handedness can be changed through the transformation $u \to 1 - u$ of the Wyckoff positions. Since $u_{Fe} + u_{Ge} \neq 1$ this transformation is not identical with an exchange of Fe and Ge. The

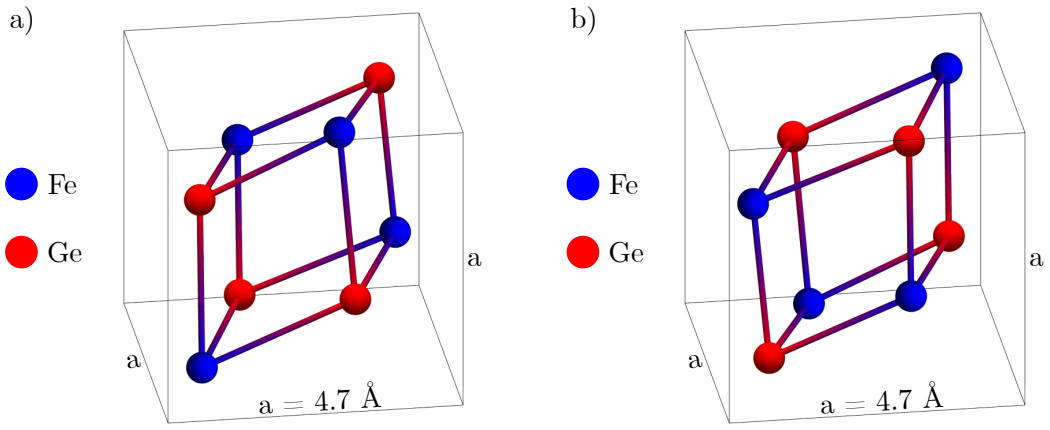

Figure 3.1.: a) and b) are the unit cells of both B20 FeGe enantiomers. The blue and red spheres denote the respective lattice sites of Fe and Ge. The length of the cell edges is $a = 4.700\,\text{Å} \pm 0.002\,\text{Å}$.

chirality in this crystall structure can be illustrated through the structural helices formed by both Fe and Ge parallel to the [111]-direction of the crystal. Helices are three-dimensional chiral objects. They are shown in Fig. 3.2 together with their rotation direction. The helices of Fe and Ge have an opposite handedness, i.e. in Fig. 3.2 a) Fe rotates clockwise and Ge rotates counter clockwise. When looking at the other enantiomere in Fig. 3.2 b), the handedness of these structural helices has switched. This means, that the distinction between Fe and Ge leads to a chiral crystal lattice. But even if Fe and Ge atoms were indistinguishable

the crystal structure would still be chiral. Due to the inequality $u_{Fe} + u_{Ge} \neq 1$, the clockwise rotating Fe helices cannot be brought to coincide with the clockwise rotating Ge helices after inversion. The same is true for the counter clockwise rotating helices. Thus, the crystal is chiral. This chirality is the origin of the DMI observed in FeGe.

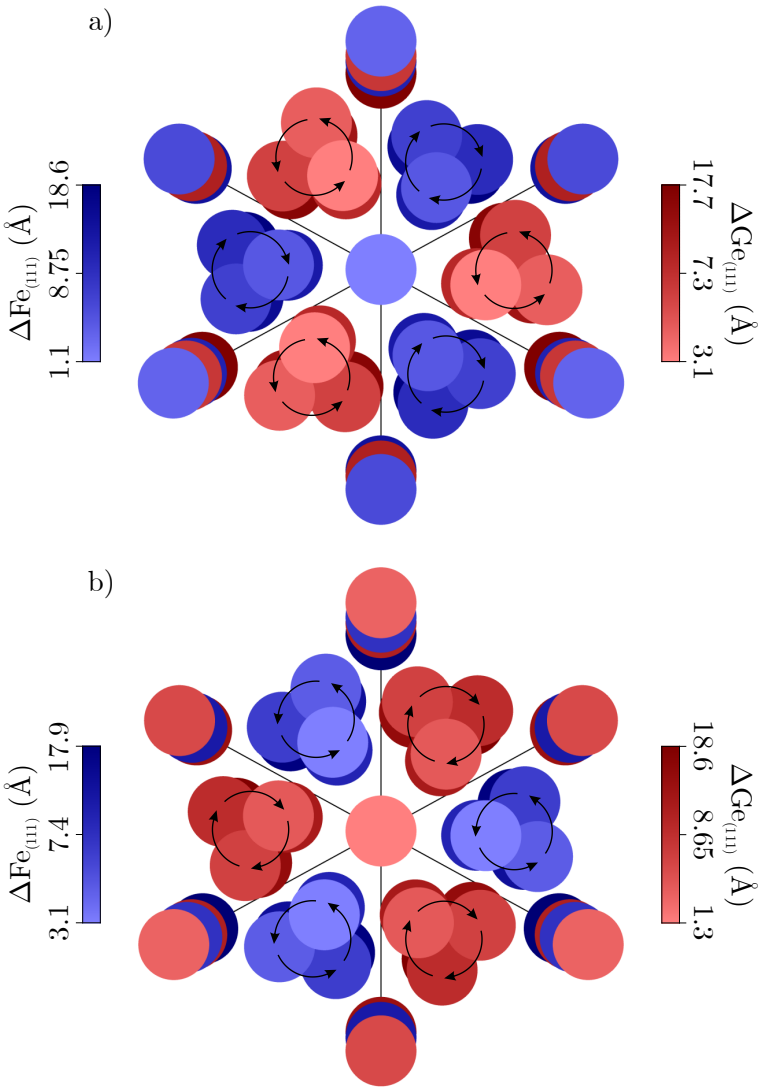

Figure 3.2.: View along the [111]-direction of the FeGe crystal lattice for both enantiomers a) and b) in Fig. 3.1. The distance from the (111)-plane placed in the front lower left corner of the cube in Fig. 3.1 is color coded. Arrows indicate the direction of rotation of helices in the crystal structure.

3.2 Magnetic Properties of B20 FeGe

In [58], magnetization measurements gave a Curie temperature of $T_C = 280\,\mathrm{K} \pm 2\,\mathrm{K}$ and an extrapolated saturation magnetization of $1.00\,\mu_\mathrm{B} \pm 0.04\,\mu_\mathrm{B}$ per iron atom. These results are consistent with Mössbauer studies [59, 60]. Other Curie temperatures were reported, for example $T_C = 278.2\,\mathrm{K}$ [61] and $T_C = 279.1\,\mathrm{K}$ [62]. The amount of different values is due to the intense research of the FeGe magnetic phase diagram, especially in the vicinity of the Curie temperature. The magnetic phase diagram mainly consists of a ferromagnetic, paramagnetic, conical, and helical phase [61]. Of particular interest is the so-called A-phase [63, 64], which was intensively studied [65, 66] and identified as a skyrmion lattice [10, 67, 68]. A complete characterization of the A-phase is still subject to magnetic research [61, 69]. However, even though the phase diagram is an important aspect of FeGe this thesis centers on results obtained in the ferromagnetic phase. In 1970 Lundgren et al. [8] published the temperature dependent magnetocrystalline anisotropy of FeGe as second order cubic anisotropy, which takes the form of Eq. 3.1 and is depicted in Fig. 3.3. Here and in the

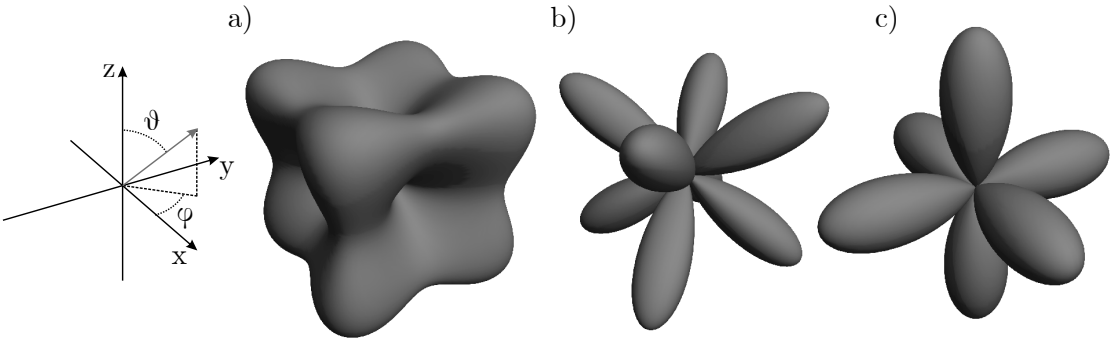

Figure 3.3.: a) and b) are the first and second order power series expansion with cubic symmetry of the free energy density. The corresponding definition can be seen in Eq. 3.1. c) is the free energy density of FeGe using Eq. 3.1 and the conditions $K_4 = -2K_6$ with $K_4 < 0$ taken from [8]. The furthest point from the origin in c) corresponds to an energy contribution of 0. An appropriate offset was introduced beforehand to be able to show the general structure and intuitively identify hard and easy axes. A coordinate system corresponding to the presented energy landscapes is depicted as an inset on the left to demonstrate the relation between Cartesian and spherical coordinates.

further course of this work $\vec{e}\,(\theta, \varphi) = (\sin(\theta)\cos(\phi), \sin(\theta)\sin(\phi), \cos(\theta))$ is the unit vector of spherical coordinates. They further report the relationship between the cubic anisotropy parameters to be $K_4 = -2K_6$ with $K_4 < 0$ for all temperatures.

$$\begin{aligned} F_\mathrm{cubic} =& K_4(T) \cdot \left(e_\mathrm{x}(\theta,\varphi)^2 e_\mathrm{y}(\theta,\varphi)^2 + e_\mathrm{x}(\theta,\varphi)^2 e_\mathrm{z}(\theta,\varphi)^2 + e_\mathrm{y}(\theta,\varphi)^2 e_\mathrm{z}(\theta,\varphi)^2\right) \\ &+ K_6(T) \cdot \left(e_\mathrm{x}(\theta,\varphi)^2 e_\mathrm{y}(\theta,\varphi)^2 e_\mathrm{z}(\theta,\varphi)^2\right) \end{aligned} \tag{3.1}$$

Previous FMR measurements on bulk cubic FeGe are dominated by four papers from S. Haraldson published with different co-authors throughout the 1970s, with the first one as early as 1971. In the latter [70] two single crystal samples of FeGe, one being a disk with 0.7 mm diameter and 0.07 mm height and the other a sphere with 0.4 mm diameter, are investigated at 9.5 GHz and 35 GHz. The obtained spectrum is interpreted as three resonance lines, with a mostly temperature independent uniform mode around 300 mT at 9.5 GHz and two strongly temperature dependent resonances interpreted as spin waves in the conical phase, the first appearing between 250 K and 150 K and the second between 150 K and 80 K. The penetration depth of the microwaves is estimated to be around 1 µm. The measured samples were provided by M. Richardson, who also gave the first description of the B20 FeGe structure [27,28]. The second [71] and third [72] publication focus on the uniform mode and the two temperature dependent resonance lines respectively. The last of the four papers [73] summarizes the to this point obtained knowledge about FeGe. With a frequency range between 3.2 GHz and 35 GHz and a temperature range between 4.2 K and 300 K a deep understanding of the magnetic properties was possible. The g-factor obtained for the uniform mode is $g = 2.07$ for all frequencies. Unidirectional anisotropy was never observed. For bulk FeGe the relaxation frequency λ is reported as $4 \times 10^9\,\mathrm{s}^{-1}$ [71], from which the damping parameter can be calculated through $\alpha = \lambda/\mu_0\gamma M$. This gives a range for the damping parameter between 0.05 and 0.09 for temperatures between 115 K and 257 K. Several values for the damping parameter α were reported for cubic FeGe and are listed in Tab. 3.1. Also multiple values for the DMI constant and the exchange stiffness are reported for thin films. A list can be found in [74]. In this thesis the values obtained by Turgut [75] are used. They were determined through temperature-dependent magnetization measurements as $A = 1.37 \times 10^{-12}\,\mathrm{J\,m^{-1}} \pm 0.13 \times 10^{-12}\,\mathrm{J\,m^{-1}}$ and $d = 2.48 \times 10^{-4}\,\mathrm{J\,m^{-2}} \pm 0.26 \times 10^{-4}\,\mathrm{J\,m^{-2}}$.

Value for α	Sample type	Temperature	Year	Source
0.28 ± 0.02	-	-	2017	[76]
0.05 - 0.09	bulk	115 K - 257 K	1974	[71]
0.0036 ± 0.0003	thin film	310 K	2017	[77]
0.038 ± 0.005	thin film	258 K	2017	[78]
0.066 ± 0.003	thin film	264 K	2017	[79]

Table 3.1.: Different damping parameters α reported in literature. The first value is the result of a finite-element based micromagnetic simulation. All other values were optained through microwave resonance experiments of FeGe.

3.3 Sample Preparation

The examined FeGe samples are all from the same batch and the same ones used in my Bachelor thesis [16], where the synthesis is described in detail. The samples were synthesized by Iliya Radulov at the Deutsches Elektronen-Synchrotron in Hamburg, using a Kawai-type [80] Multianvil Apparatus with Waker-type module [81]. First, stoichiometric FeGe was melted three times by induction heating and then annealed at 1000 K for 130 h. Afterwards, a high pressure high temperature synthesis was undertaken at 7 GPa and 1075 K on a machined cylindrical sample. The brittle sample broke into smaller pieces during removal. These smaller parts were not altered any further so the samples retain their broken edges.
In this thesis three different samples are used. A "disk shaped" sample (Fig. 3.5) for crystallography, an "L-shaped" sample (Fig. 4.1) for angular dependent FMR and a "cylindrical" sample (Fig. 4.9) for temperature dependent FMR and magnetometry measurements.

3.4 X-ray Diffraction Measurements

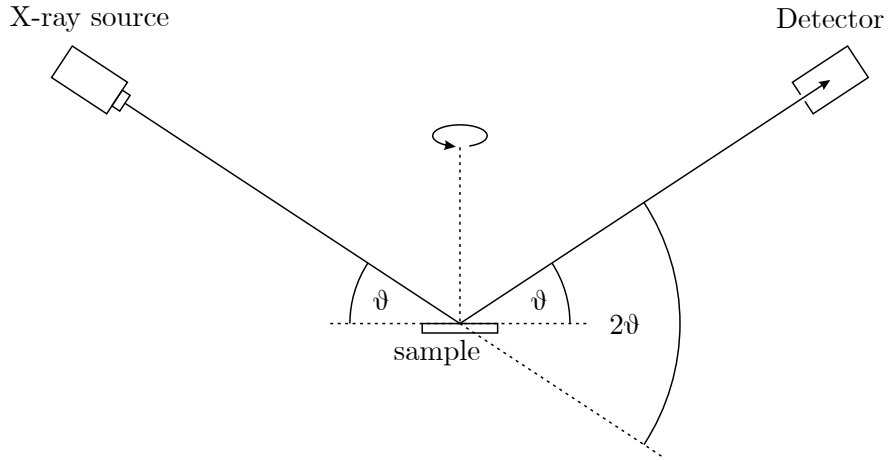

Figure 3.4.: Schematic illustration of a XRD experiment with Bragg-Brentano geometry. Light from a X-ray source hits the (in this case spinning) sample under the angle θ, which is also the exit angle at which a detector measures the diffracted light. Therefore the angle between incident and diffracted light is 2θ. In the course of the experiment θ is varied. The zero-background sample holder is not depicted.

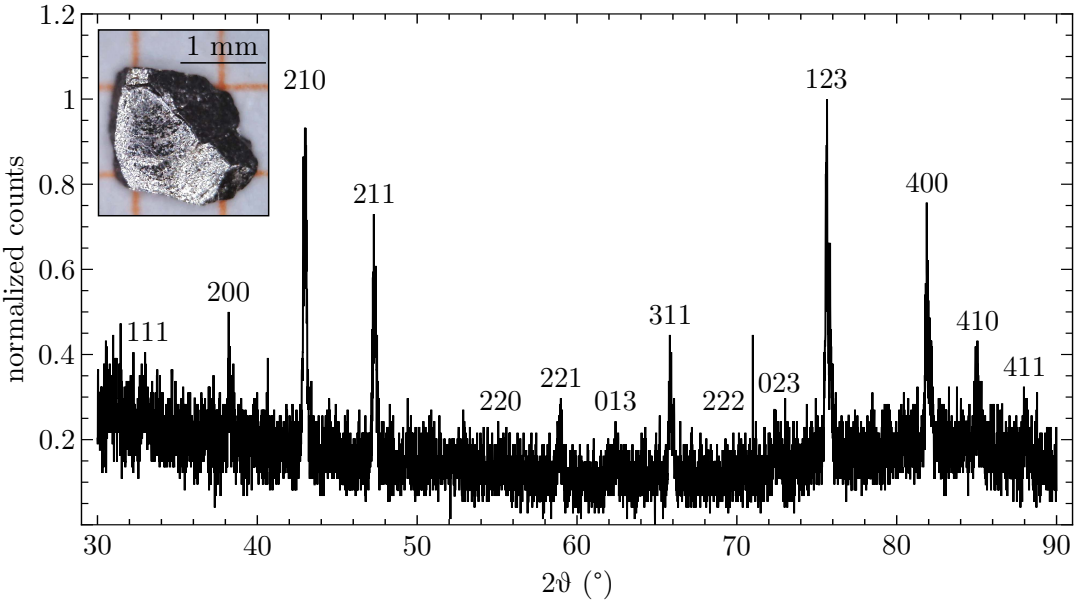

Figure 3.5.: XRD spectra of the "disk shaped" FeGe sample. The drawn in crystallographic planes of cubic FeGe can be calculated with Eq. 3.2 and the lattice parameter of cubic FeGe introduced in Sec. 3.1. An inset in the upper left corner shows an optical microscope image of the sample.

X-ray diffraction (XRD) is a standard technique of crystallography and allows to investigate the crystall structure of a sample. For this it uses the aligned planes formed by atoms inside a crystall lattice to impose a path difference between X-rays diffracted at different levels of the planes. This path difference is tuned by the incident angle θ of the X-rays until constructive interference occurs and a maximum of intensity can be measured at an exit angle which is equal to the incident angle. The angle can be calculated using Bragg's law [82], written as

$$\lambda = 2p_{hkl}\sin\left(\theta_{\mathrm{B}}\right). \tag{3.2}$$

λ is the wavelength of the X-rays, p_{hkl} the separation of the respective aligned planes, and θ_{B} the incident angle of constructive interference. To differentiate between planes, the Miller indices hkl are used [83]. The separation of the planes p_{hkl} can then easily be calculated as

$$p_{hkl} = \frac{a}{\sqrt{h^2 + k^2 + l^2}}. \tag{3.3}$$

Here a is the lattice parameter [84, p.4]. In a powder or perfectly polycrystalline sample all possible Bragg diffraction peaks can be measured, since every orientation of the crystal is present. A difference of intensity between a powder and a sample spectrum can then reveal possible texturations in the sample. X-Ray diffraction was measured with the help of Mehmet Acet in a Phillips PANalytical X'Pert PRO on a "disk shaped" FeGe sample. The

sample was spinning during the measurement, self-defeating when looking for texturation, but necessary to minimize the effects of the irregular surface. For that it was placed with vacuum grease on a zero-background sample holder. The angle steps were $\Delta 2\theta = 0.001°$. Non-monochromatized X-rays from a Cu X-ray source were used in a Bragg-Brentano geometry [85], which is depicted in Fig. 3.4. The results can be seen in Fig. 3.5. Due to the small sample size and an irregular surface the sample is hardly suitable for XRD measurements. Nevertheless diffraction peaks are visible in the spectrum. All peaks consisting of more than one data point can be associated with a crystallographic direction of cubic FeGe. Therefore it can be assumed, that cubic FeGe is the only ordered crystal structure in the sample. This doesn't include amorphous structures or local variations of compositions, which this measurement technique isn't sensitive for. A comparison of peak intensities to find a potential texturation is not possible, due to the already mentioned spinning sample. The Scherrer equation [86] is also not applicable for the determination of the crystallite size, due to its upper size limit of about 100 nm.

4 Dynamic Unidirectional Anisotropy

4.1 Angular Dependent Ferromagnetic Resonance

For a better understanding of the magneto-dynamic properties of FeGe it is imperative to know the energy landscape of the magnetization, which is described by the free energy density introduced in Sec. 2.1. A measurement technique to obtain this information is FMR. One way to perform an FMR measurement is to measure the magnetic field dependent microwave reflection of a resonator, in which the sample is placed. When the sample is in resonance, the resonator is detuned, which can be measured as an increased microwave reflection [20, p. 12]. The sensitivity of the measurement can be increased through the usage of a magnetic field modulation, whilst its frequency is the reference signal to a Lock-In amplifier. This results in the measurement of the differentiated resonance spectrum. FMR measurements were performed with a conventional Bruker X-band FMR spectrometer using a cylindrical TE_{011} cavity. The sample was a millimeter sized "L-shaped" polycrystalline FeGe flake weighing 17.0 mg $\pm$ 0.5 mg, which is depicted in Fig. 4.1. Since FeGe is not ferromagnetic at room

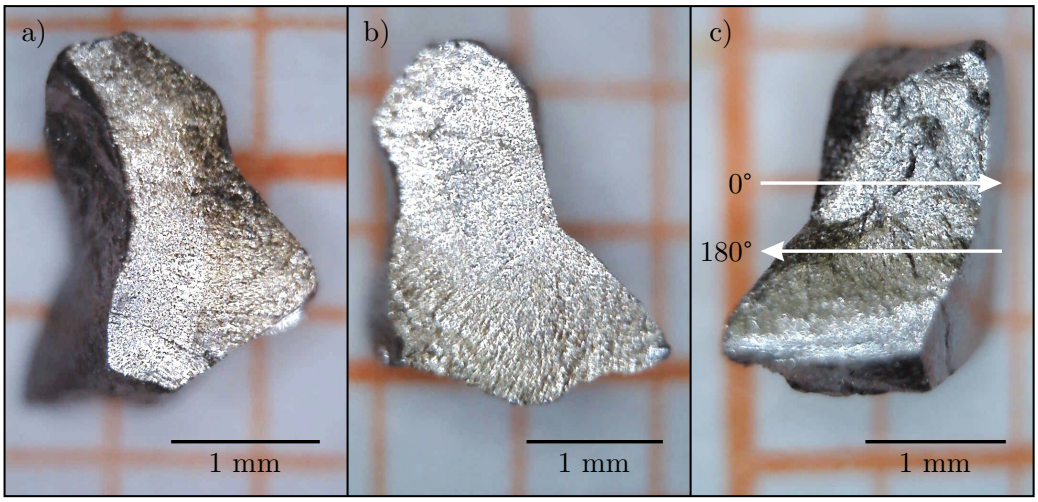

Figure 4.1.: Optical microscope images of the "L-shaped" FeGe sample, which was used for the angular dependent FMR measurements in this thesis. The images show the front a), back b) and side c) of the sample. The front points to the right in image c). In frame c) the respective 0° and 180° magnetic field directions of the FMR measurements are shown. The axis of rotation in the measurement lies perpendicular to the arrows in the image plane.

temperature, the sample had to be cooled for measurements. Therefore, a cooling system based on liquid nitrogen was installed into the FMR equipment. The liquid nitrogen inside a vacuum insulated can was evaporated with a fixed heating voltage and then transported

through a transfer line into a glass tube, which was mounted inside the cavity. On the way the gas passed a heating coil and a temperature sensor. The voltage applied on the heating coil was controlled by a proportional–integral–derivative controller (PID) comparing a chosen temperature setpoint to the measured temperature at the sensor. The temperature sensor itself had to be fixed a few centimeter below the sample outside the cavity to not disturb the measurement. The total temperature error is assumed to be as high as $\pm\,^{5\,\mathrm{K}}_{2\,\mathrm{K}}$. The error is asymmetric, due to a further warming of the nitrogen gas between temperature sensor and sample. The relative temperature error between two measurements at the same temperature can be neglected. With this setup a temperature range between 120 K and 700 K is accessible. To guarantee a successful measurement one has to be sure that the system reached a thermal equilibrium by allowing for enough adjustment time. To be able to evaluate the FMR results, the sample is approximated as a flat cylinder. When the magnetic field lies in the base plane, the direction is called in-plane (ip) and when its perpendicular to the base plane its called out-of-plane (oop). In Fig. 4.2 the recorded FMR spectra can be seen as a contour plot. The temperature was $T = 275\,\mathrm{K} \pm\,^{5\,\mathrm{K}}_{2\,\mathrm{K}}$. A time constant of 40.96 ms and a conversion time of 81.92 ms were used together with a microwave power of 0.62 mW. The modulation frequency was 100 kHz with a modulation amplitude of 1×10^{-3} T. The positions of maximum microwave reflection are marked with yellow dots, which are, due to the asymmetric line shape (see Sec. 2.3.1) not identical with the resonance field. However, they follow the same angular symmetry as the resonance field. Due to the polycrystallinity of the sample one would expect that the only angular change of the resonance field is caused by the shape anisotropy of the sample explained in Sec. 2.2.2. The angular dependence indeed shows a uniaxial anisotropy contribution with a maximum resonance field position in the oop-direction (by definition 0° and 180°) and a minimum resonance field in the ip-direction of the sample. But additionally, the resonance field at 180° is lower than at 0°, thus there is a unidirectional anisotropy, i.e. a shift of the resonance field after magnetic field inversion (see Fig. 4.3). Through the assumption of a free energy density model one can now extract sample parameters like the demagnetization tensor and quantify the strength of the unidirectional anisotropy. The model is

$$F = \underbrace{\vec{M} \cdot \vec{B}_{UD}}_{\text{unidirectional anisotropy}} \underbrace{+ \frac{\mu_0}{2} \cdot \vec{M} \cdot \boldsymbol{N} \cdot \vec{M}}_{\text{shape anisotropy}} \underbrace{- \vec{M} \cdot \vec{B}}_{\text{Zeeman term}} . \tag{4.1}$$

The energy contribution of the unidirectional anisotropy in this model is the scalar product of the normalized magnetization with a phenomenologically motivated unidirectional anisotropy field $\vec{B}_{UD}$ imposing a one fold symmetry on the system. In the measurement the unidirectional axis lies along the oop-direction of the flat cylinder, which is from now on per definition the z-direction of the coordinate system. This leads to a unidirectional anisotropy field of $\vec{B}_{UD} = (0, 0, {}^{K_{UD}}/_{M})$, where K_{UD} is the unidirectional anisotropy constant. The de-

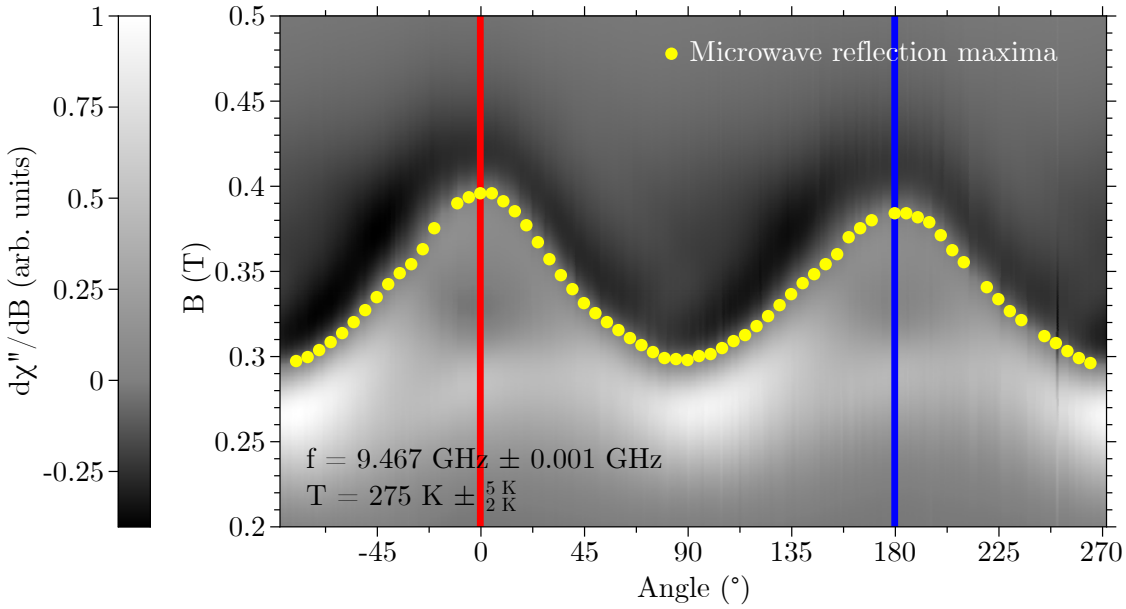

Figure 4.2.: Contour plot of the angular dependent FMR spectra. The sample was rotated from ip to oop, while 0° and 180° denote the oop-directions. The frequency was $f = 9.467\,\mathrm{GHz} \pm 0.001\,\mathrm{GHz}$ at a temperature of $T = 275\,\mathrm{K} \pm {}^{5\,\mathrm{K}}_{2\,\mathrm{K}}$. A linear background was subtracted. The yellow dots indicate the zero crossing of a resonance spectrum, which corresponds to the maximum microwave reflection. For improved clarity only every fifth maximum is depicted. The red and blue lines indicate the respective resonance spectra depicted in detail in Fig. 4.3. They are 180° degree apart from each other, which is identical to a magnetic field inversion.

magnetization tensor $\boldsymbol{N}$ can be calculated using the equivalent ellipsoid proposed by Beleggia et al. [41]. The z-component then becomes

$$\boldsymbol{N}_{zz} = 1 + \frac{\tau}{\pi}\left(1 + \log\left(\frac{\tau^2}{16}\right)\right) + \mathcal{O}\left(\tau^3\right) \tag{4.2}$$

with $\boldsymbol{N}_{xx} = \boldsymbol{N}_{yy}$ and $1 - \boldsymbol{N}_{zz} = 2 \cdot \boldsymbol{N}_{xx}$. Here $\tau = {}^{h}/_{2r}$ is the aspect ratio with the height h and the diameter $2r$ of the cylinder. We can now express Eq. 4.1 in spherical coordinates taking our considerations into account, which results in

$$\begin{aligned} F_S = &- K_{UD} \cdot \cos(\theta) + n \cdot \frac{\mu_0}{2} \cdot M^2 \cdot \cos(2\theta) \\ &- M \cdot B \cdot (\cos(\theta)\cos(\theta_B) + \cos(\phi - \phi_B)\sin(\theta)\sin(\theta_B)) . \end{aligned} \tag{4.3}$$

The angles (θ, ϕ) are the angles of the magnetization and (θ_B, ϕ_B) the angles of the external magnetic field. The constant n is a factor scaling the demagnetization and is linked to the aspect ratio of the cylinder by $n = {}^{(2\pi+3\tau+3\tau\log({}^{\tau^2}/_{16}))}/_{4\pi}$. Terms not dependent on the magnetization angles were ignored. This model is used to fit the experimental angular dependence

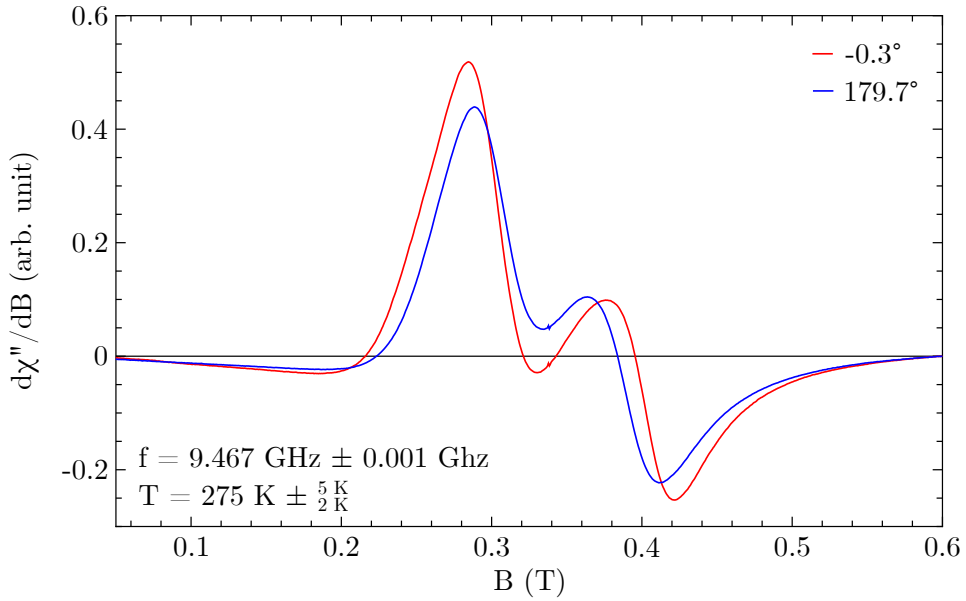

Figure 4.3.: Comparison between ferromagnetic resonance spectra at $-0.3°$ and $179.7°$. The frequency was $f = 9.467\,\mathrm{GHz} \pm 0.001\,\mathrm{GHz}$ at a temperature of $T = 275\,\mathrm{K} \pm {}^{5\,\mathrm{K}}_{2\,\mathrm{K}}$. The general lineshape of FeGe visible in this Figure is discussed in Sec. 4.5.1.

of the FMR data. A Mathematica program written by Benjamin Zingsem [47] was used. It solves Eq. 2.15 for a given set of magnetic field angles and minimizes the difference to an interpolation of the measured data by varying the parameters. Due to the variety of damping parameters α reported in literature (see Sec. 3.2), for most of which $\alpha \ll 1$, the limiting case $\alpha \to 0$ was chosen for these calculations. A set of start values has to be passed to the program beforehand. To solve the equation, the angles of the magnetization have to be known. Therefore the free energy density is minimized with regards to the magnetization angles, while the magnetic field is assumed to be the measured resonance field. The

	Value	Error
K_{UD}	$873\,\mathrm{J\,m^{-3}}$	$\pm 175\,\mathrm{J\,m^{-3}}$
n	0.37	± 0.01
t	$0.015\,\mathrm{T}$	$\pm 0.001\,\mathrm{T}$

Table 4.1.: Fit parameters (Fig. 4.4) of the angular dependent FMR measurement (Fig. 4.2) of the "L-shaped" FeGe sample (Fig. 4.1). The errors were estimated in such a way, that with the other parameters fixed a change of the respective parameter by its error yields a mean difference between fit and data, which is 1.1 times the original difference.

fitparameters were K_{UD}, n and an additional value t shifting every zero crossing position

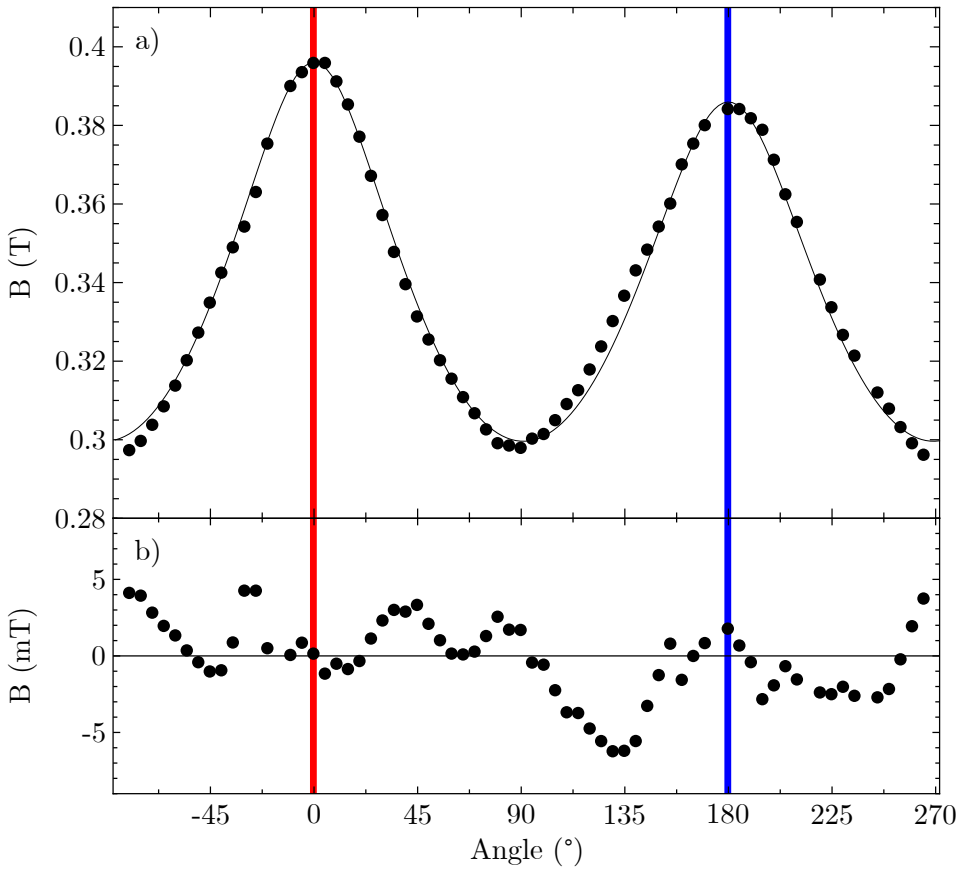

Figure 4.4.: a) Comparison between the fit (see text) and the angular dependent FMR-measurement in Fig. 4.2. Only every fifth data point is plotted for clarity. b) Difference between the fit and the data points in a). In a perfect fit these points should follow a Gaussian distribution around 0 T. The red and blue lines indicate the angles of the respective resonance spectra depicted in Fig. 4.3.

by the same amount to compensate for the asymmetry of the lineshape. The magnetization of $M = 98\,380\,\mathrm{A\,m^{-1}}$ was taken from temperature dependent magnetization measurements from a different sample of the same synthesis process at 275 K, which are discussed in the next section. The obtained values can be found in Tab. 4.1 and the corresponding comparison between fit and measurement in Fig. 4.4. The factor $n = 0.37$ corresponds to an aspect ratio of $\tau = 0.08$, meaning that the diameter of the cylinder is roughly 10 times the height, which does not agree with the sample shape in Fig. 4.1. The in Sec. 4.5 discussed lineshape suggest a distribution of resonance lines rather than a single individual line, while the highest contribution to this broadening is shown to stem from inhomogeneous demagnetization fields inside the sample. The analysis of the angular dependent FMR position as done in this section assumes that the point of highest amplitude always refers to the same part of the sample. The value of n only describes the shape anisotropy of this part of the sample.

Due to the penetration depth of the microwaves of 1 µm [70] the shape anisotropy can not easily be determined from the general sample shape.
This section shows, that angular dependent FMR measurements of FeGe display a unidirectional anisotropy. A phenomenological unidirectional magnetic field can be used to quantify the strength of this effect. Such a field could be explained by exchange bias, which is further discussed of the next section.

4.2 Vibrating Sample Magnetometry

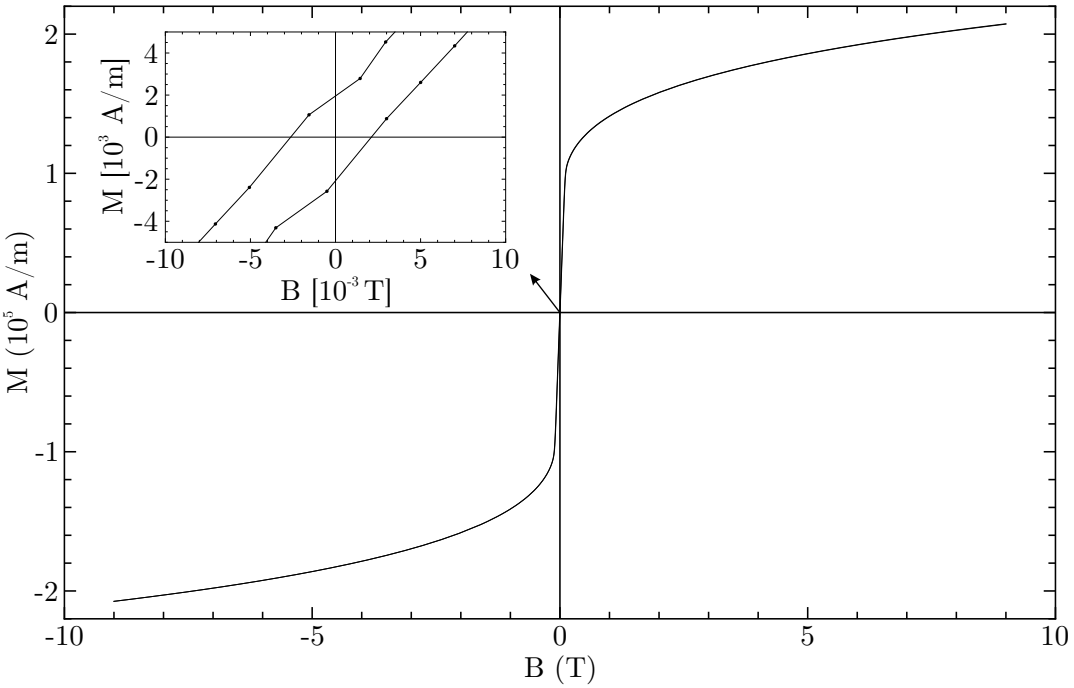

Figure 4.5.: Hysteresis loop of FeGe between 9 T and −9 T measured at 275 K via vibrating sample magnetometry (VSM). The measurement was performed along the unidirectional axis, in this case the out-of-plane orientation, identified before using FMR. The inset depicts a detailed view in the vicinity of 0 T. No significant shift, i.e. exchange bias, can be seen.

Unidirectional anisotropy can be caused by exchange bias [24]. Hysteresis loops obtained along the unidirectional axis of the sample can be used to check whether any asymmetry in the magnetization is present. The "L-shaped" sample discussed in the last section was destroyed in the process of this work and couldn't be used for these measurements. A "cylindrical" FeGe sample produced in the same synthesis process, which is depicted in Fig. 4.9, was taken instead. The unidirectional axis was identified as the oop-direction beforehand through FMR measurements, which are shown in Fig. A.1. Hysteresis and temperature

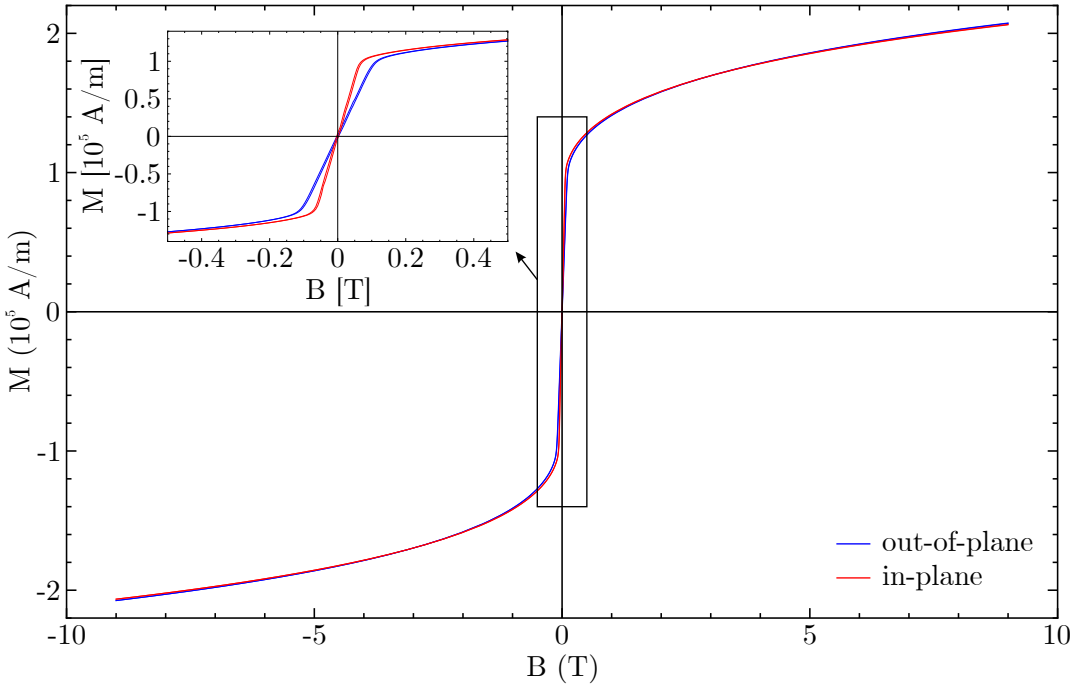

Figure 4.6.: Hysteresis loop along the out-of-plane (hard axis) (blue) and in-plane (easy axis) (red) directions of FeGe between 9 T and −9 T measured at 275 K via VSM. The inset depicts the framed area inside the plot.

dependent magnetization curves were then obtained through VSM [87] by Marina Spasova. This technique measures the voltage induced inside pickup coils by the magnetic stray field of a vibrating sample. This voltage can then be associated with a certain absolute magnetic moment. It is common to calculate the magnetization, which is the magnetic moment per volume, through division with the sample weight and multiplication with the density. The hysteresis loop of FeGe at 275 K can be seen in Fig. 4.5. Evidently no exchange bias or additional asymmetry is present. Since the unidirectional axis coincides with the magnetic hard axis in this case, an additional hysteresis loop along the easy axis can be used to determine the magnetic anisotropy energy density (MAE), which is the difference between the areas below the curves. In Fig. 4.6 both hysteresis loops can be seen. Along the hard direction a larger magnetic field is needed to saturate the sample. Accordingly, the hysteresis loop of the hard axis can be identified as the one with saturation at higher fields. Both hysteresis loops saturate in a linear dependence with almost identical slopes. The hysteresis is closed after 200 mT, yet the magnetization is still rising. This can happen in a pure ferromagnet along the hard axis. Then the magnet moments are all aligned, but point along an intermediate direction, which is energetically favorable. However, in this case both the hard axis and the easy axis show this phenomenon equally, therefore an additional

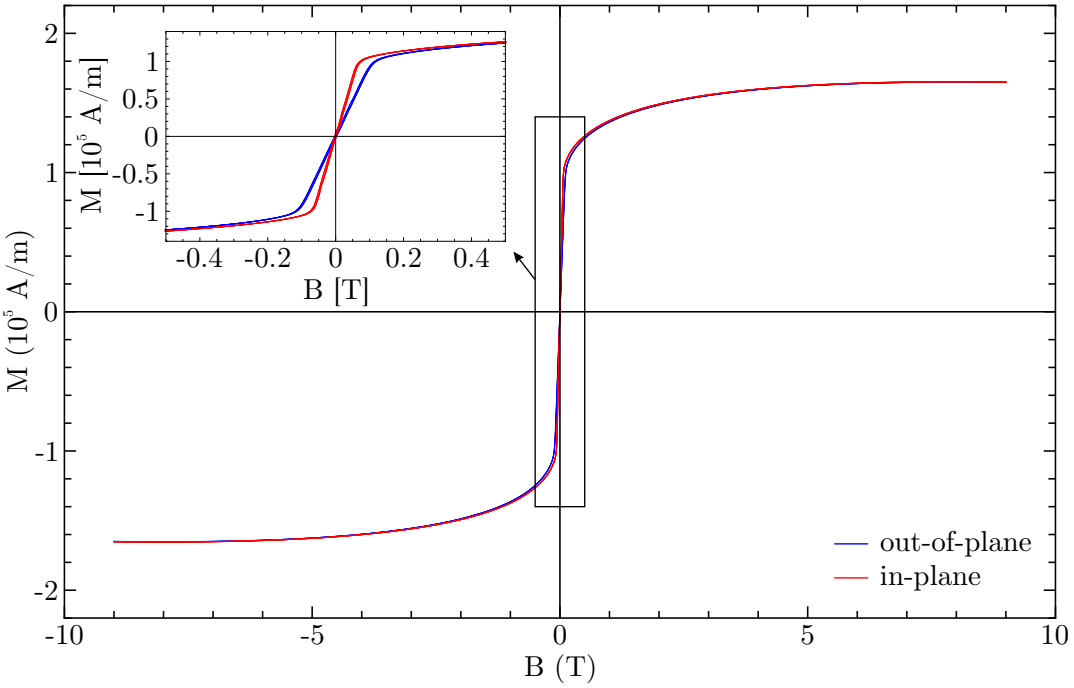

Figure 4.7.: Hysteresis loops of Fig. 4.6 after compensation of the linear contributions.

contribution to the magnetization must be considered and subtracted as a linear fit before the MAE can be determined through integration. This has been done in Fig. 4.7. The difference between the numeric integration of both curves gives the MAE:

$$E_{\mathrm{MAE}} = 13\,600\,\mathrm{J\,m^{-3}} \pm 400\,\mathrm{J\,m^{-3}}$$

The error stems from the standard error of the linear model fit. The MAE can now be used to calculate the difference of the resonance fields in a saturated system between the hard and easy axis. For this purpose it must be divided by the saturation magnetization M_{VSM}:

$$M_{\mathrm{VSM}} = 165\,177\,\mathrm{A\,m^{-1}} \pm 74\,\mathrm{A\,m^{-1}}$$

Then the field difference ΔB_{VSM} can be calculated as

$$\Delta B_{\mathrm{VSM}} = \frac{E_{\mathrm{MAE}}}{M_S} = 82.3\,\mathrm{mT} \pm 2.4\,\mathrm{mT}. \tag{4.4}$$

The only anisotropy expected for static magnetometry measurements of polycristalline FeGe is shape anisotropy. Therefore the value of ΔB_{VSM} in Eq. 4.4 should give the difference between the easy and hard direction in an FMR measurements at 275 K of the “cylindrical” FeGe sample. Due to its dependence on the shape it is only valid for this particular sample.

However, the highest measured difference between the easy and hard direction in the angular dependent FMR measurements of the "L-shaped" sample is $\Delta B_{\mathrm{FMR}} = 100\,\mathrm{mT} \pm 1\,\mathrm{mT}$, which is the same order of magnitude as the calculation from VSM measurements. While

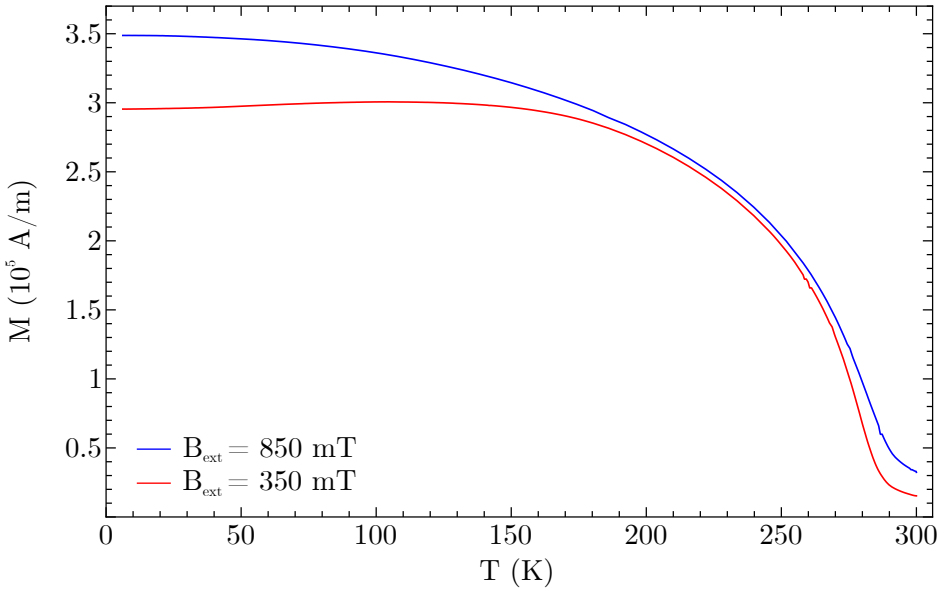

Figure 4.8.: Temperature dependent magnetization of the FeGe sample shown in Fig. 4.9. The magnetization was measured along the hard direction of the sample at a constant magnetic field of both 850 mT (blue) and 350 mT (blue). The measurement was performed from high to low temperatures. The plot follows the typical shape of a ferromagnetic magnetization below the Curie temperature.

hysteresis measurements along the easy and hard axis at a certain temperature are important for comparison with angular dependent FMR measurements a temperature dependent magnetization measurement is important for comparison with temperature depentend FMR measurements. Therefore temperature dependent magnetization measurements were performed at both $B_{\mathrm{ext}} = 350\,\mathrm{mT}$ and $B_{\mathrm{ext}} = 850\,\mathrm{mT}$ for comparison with the X-band and K-band FMR measurements respectively. To measure roughly at the same external magnetic field as the resonance field in FMR is important, due to the field dependence of the magnetic phase diagram. The temperature dependent FMR measurements were all performed with the external field pointing along the hard axis, which is also the unidirectional axis. This can cause an additional error in magnetization measurements, due to the already mentioned energetically favorable intermediate direction of the magnetization, which can occur. Figure 4.7 demonstrates, that above $B_{\mathrm{ext}} = 200\,\mathrm{mT}$ at 275 K this error becomes negligible. The measurement at both external fields can be seen in Fig. 4.8. The biggest differences between both curves are at temperatures below 180 K, where the already mentioned hard axis effects come into play at 350 mT and above 270 K, where the phase transition to paramagnetism begins.

4.3 Temperature Dependent Ferromagnetic Resonance

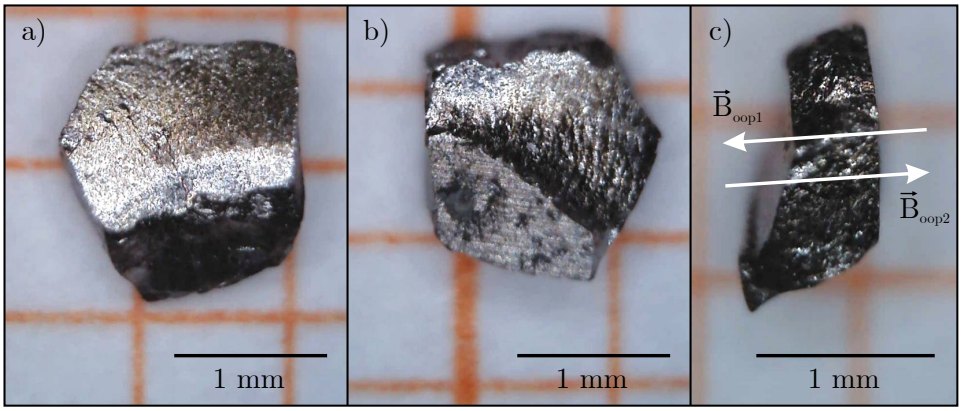

Figure 4.9.: Optical microscope images of the "cylindrical" FeGe sample used for temperature dependent FMR and magnetometry measurements. The images show the front a), back b) and side c) of the sample. The front points to the right in image c). In frame c) the respective oop-directions $\vec{B}_{oop1}$ and $\vec{B}_{oop2}$ for the magnetic field as they are called from now on are depicted.

An insight into the temperature dependence of the unidirectional anisotropy is critical for the further understanding of this effect. Therefore the resonance spectrum was measured for opposite magnetic field directions at different temperatures. For this the axis with the highest unidirectional anisotropy, identified as the oop-direction in FMR measurements (as can be seen in Fig. A.1) of the "cylindrical" FeGe sample (Fig. 4.9), was chosen. Since only the two oop directions of the external field are measured and discussed they are denoted as oop-direction 1 and oop-direction 2 as depicted in the figure. The temperature has to be changed in consecutive temperature steps for the whole measurement, because of possible magnetic phase transitions. For the same reason overshoots in temperature have to be avoided. For convenience, the temperature is set to the respective value and then both directions are measured in direct succession. This also avoids an additional temperature error. Figure 4.10 shows exemplary one of the hard-axis FMR spectra along oop-direction 1. It was obtained at a temperature of $T = 130\,\mathrm{K} \pm {}^{5\,\mathrm{K}}_{2\,\mathrm{K}}$ and a X-band microwave frequency of $f = 9.4394\,\mathrm{GHz} \pm 0.0001\,\mathrm{GHz}$. For every temperature a modulation frequency of 100 kHz was used with a modulation amplitude of $1.5 \times 10^{-3}\,\mathrm{T}$. The time constant was 10.24 ms with a conversion time of 20.48 ms and a microwave power of 1.975 mW. The spectrum is disturbed by two different contributions. The first one are resonances in the helical/conical phase mentioned in Sec. 3.2, which are strongly temperature dependent. The second one is the unusual broad lineshape of the uniform resonance, which is discussed later in Sec. 4.5. One characteristic of the resonances in the helical/conical phase is its restriction on those,

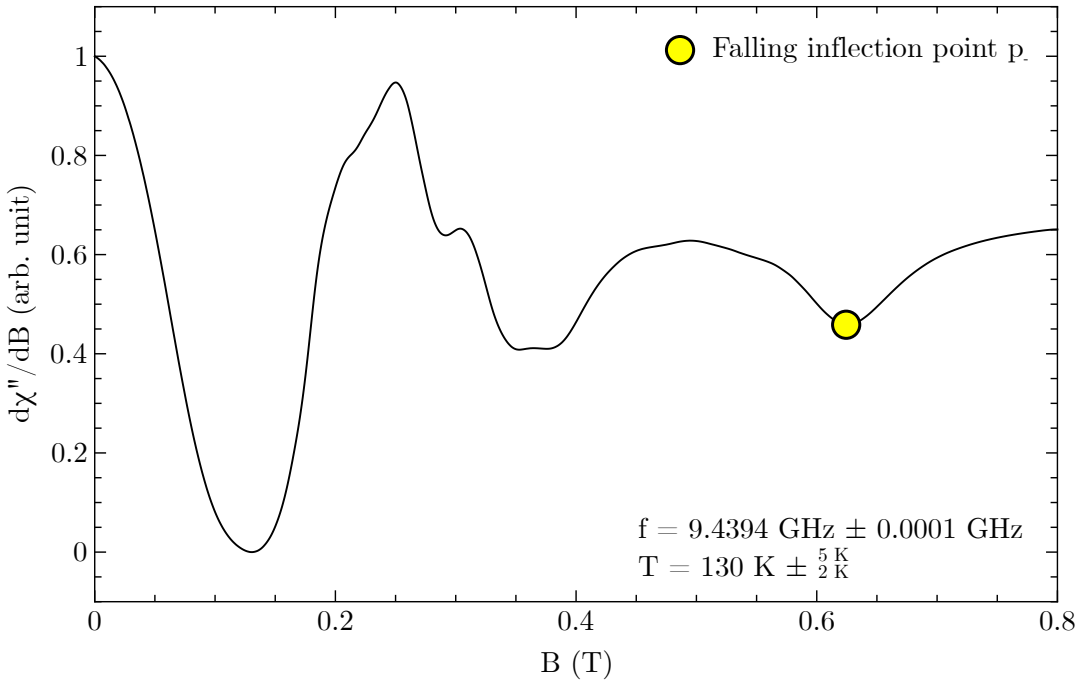

Figure 4.10.: X-band FMR spectrum with the magnetic field pointing along the hard axis/oop direction measured at $T = 130\,\mathrm{K} \pm \frac{5\,\mathrm{K}}{2\,\mathrm{K}}$, $f = 9.4394\,\mathrm{GHz} \pm 0.0001\,\mathrm{GHz}$. The measurement was done four times and then averaged to account for small temperature oscillations around the setpoint. The yellow dot indicates the inflection point p_- (see text).

i.e. it is always at lower fields than the uniform resonance mode in the ferromagnetic state. Due to the disturbed lineshape it is not possible to identify any Lorentzian or Dysonian line in the data, which were introduced in Sec. 4.5.1. A different approach is to select a certain feature in the spectrum, which is visible at every temperature and at a high enough field to be outside of the helical/conical phase. This feature is then tracked temperature dependent and can nevertheless provide useful information about the unidirectional anisotropy. Here, the local minimum associated with the highest field position of the differentiated resonance curve was chosen. It is the inflection point of the resonance curve and from now on called p_- (see yellow dot in Fig. 4.10). FMR measurements were performed between 130 K and 280 K for oop-direction 1 and oop-direction 2. The resulting contour plot of the differentiated FMR spectra can be seen in Fig. 4.11. The respective amplitude minima associated with the highest field position is marked with a yellow dot in every spectrum. The temperature dependent behaviour of p_- is typical for the hard axis of a polycrystalline ferromagnet below the Curietemperature, which is further explained in Sec. 4.5. Due to shape anisotropy, whose energy contribution is proportional to the squared magnetization (Eq. 2.8), the temperature

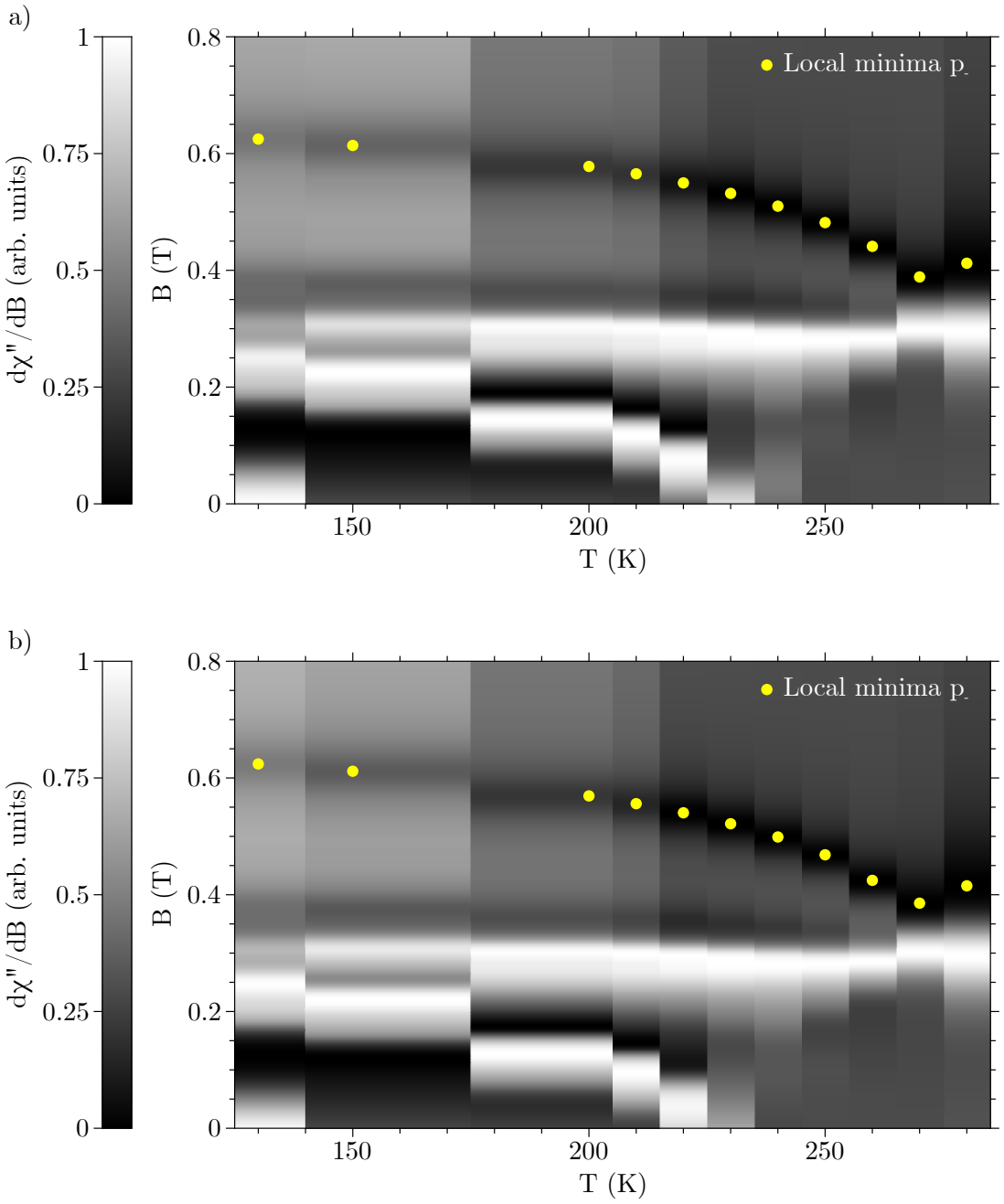

Figure 4.11.: FMR spectra as a grayscale contour plot as a function of the external magnetic field and the temperature for a) oop-direction 1 and b) oop-direction 2. The temperature was lowered with the progression of the experiment. All frequencies of the spectra lay in an interval of 5 MHz around 9.436 GHz. The gray scale is depicted on the left side of each plot. Yellow dots are used to indicate the high field inflection points of the resonance curve as explained in the text. Below 0.3 T the strongly temperature dependent resonances of the helical/conical phase are visible for temperatures below 260 K.

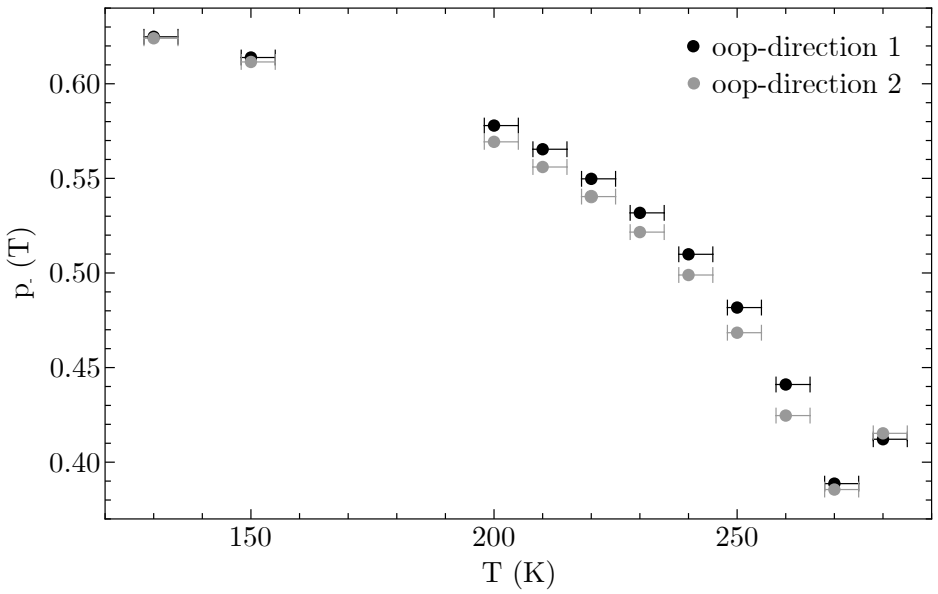

Figure 4.12.: The feature positions p_ extracted from Fig. 4.11 depicted in detail. The position is the amplitude minimum associated with the highest field position, which is the inflection point of the resonance curve. p_ of oop-direction 1 and oop-direction 2 are compared. The field difference between both directions is due to unidirectional anisotropy. The switching of oop-direction 1 and oop-direction 2 at $T = 280\,\mathrm{K} \pm \frac{5\,\mathrm{K}}{2\,\mathrm{K}}$ is due to the broadening of the resonance line at higher temperatures.

dependence of p_ follows roughly the temperature dependence of the magnetization, which is depicted in Fig. 4.8. Other contributions like the changed equilibrium position of the magnetization must also be taken into account, but play a minor role in the overall behavior. The change of direction of p_ at 280 K is due to the choice to track the inflection point. While getting closer to the Curie temperature, the FMR resonance line broadens [22, p. 770] and therefore also shifts the inflection point away from the resonance field. That means that even when the field difference of the inflection points is 0 mT unidirectional anisotropy can still be present for the resonance position. p_ for oop-direction 1 and oop-direction 2 can be seen in detail in Fig. 4.12. The measurement not only exhibits unidirectional anisotropy, but also shows a temperature dependence of the magnetic field difference between p_ of both directions at the same temperature. When p_ of oop-direction 1 is subtracted from oop-direction 2 Fig. 4.13 is obtained, which gives the temperature dependent unidirectional field difference Δp_. Starting from 130 K the difference gets larger until a reversal point around 260 K with a difference of $\Delta\mathrm{p\_} = 16.4\,\mathrm{mT} \pm 1\,\mathrm{mT}$, from which on a fast decline with a zero-crossing follows. The zero-crossing could give rise to the assumption of an inversion

of the unidirectional anisotropy. However, in the next section its origin is identified to be the broadening of the resonance line at higher temperatures.

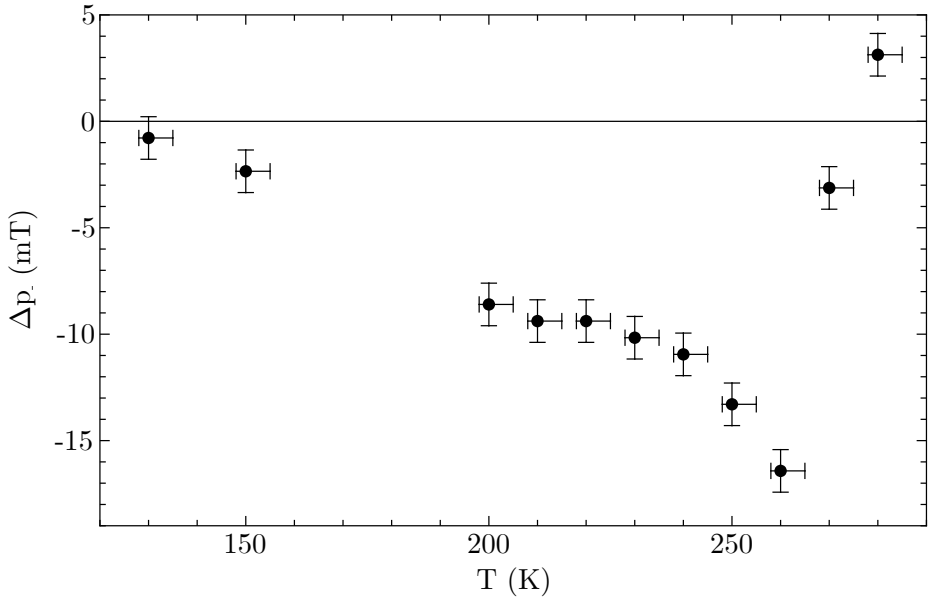

Figure 4.13.: Temperature dependent difference Δp_- of p_- between oop-direction 1 and oop-direction 2 from Fig. 4.12. Note, that this plot does not show the difference of the resonance field, but the differences of the inflection points.

4.3.1 Introduction of a Magnetization-Dependent Temperature Model

In the last section the deviation in the resonance spectrum of oop-direction 1 compared to oop-direction 2 (Fig. 4.12) was described through a field offset, which can be seen in Fig. 4.13. The behavior of this offset can also be explained by a temperature offset. It could for example occur due to asymmetric microwave heating. If this is true one should be able to reproduce the function course of Fig. 4.13 by using only one temperature dependent FMR measurement, w.l.o.g of oop-direction 1, and an additional temperature offset. Due to our limitation to discrete temperature steps in a finite measurement one has to interpolate the data first. The interpolation for oop-direction 1 can be seen in Fig. 4.14. In this model $B_{oop1}(T)$ corresponds to oop-direction 1 and $B_{oop1}(T + \Delta T)$ would then correspond to oop-direction 2. Therefore with the right ΔT Fig. 4.13 should follow the difference $B_{oop1}(T + \Delta T) - B_{oop1}(T)$ between them. A look at Fig. 4.12 alone shows that a temperature difference, which corresponds to an arbitrary shift in the horizontal axis for each point, is able to bring both directions to coincide in the same way an arbitrary vertical shift does. One can now calculate the temperature

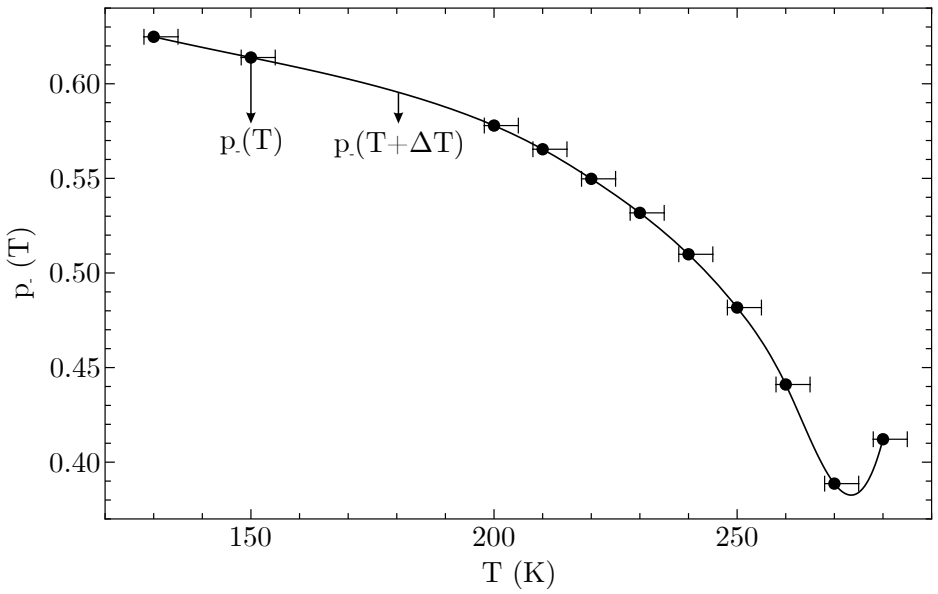

Figure 4.14.: Spline interpolation of the temperature dependent position of p$_-$ of oop-direction 1, which is depicted in Fig. 4.12, together with the actual data points. The idea of a temperature offset is illustrated by displaying p$_-$ extracted from the interpolation with and without offset.

difference necessary to obtain Fig. 4.13. It is plotted in Fig. 4.15. The temperature difference ΔT between both oop-directions rises with falling temperature beginning at 280 K with a shoulder at 250 K until it reaches a maximum at around 200 K with $\Delta T = 7.1\,\mathrm{K} \pm 0.8\,\mathrm{K}$. After that it begins to fall again for lower temperatures. Through the tracking of a feature position, which is sensitive to temperature change, instead of a real resonance field, it is possible to accurately determine the temperature change in the sample without worrying about otherwise important factors like lineshape, resonance distributions or resonance line distortions. This temperature change can also explain the zero-crossing of the field difference seen in Fig. 4.13. As already explained the FMR resonance line broadens while getting closer to the Curie temperature. Due to the evaluation of the inflection point this broadening has a higher impact on p$_-$ at high temperatures than the shift of the resonance position. Later in this work this temperature change is explained as asymmetric microwave heating due to magnon-scattering. The downside of the feature position choice is a possible field dependence of the unidirectional anisotropy. Since the unidirectional anisotropy is explained by effects related to the resonant absorption of the microwaves, it is expected to become stronger with larger amplitude of the resonance curve, that is more absorbed microwave power. The temperature difference shown in Fig. 4.15 should be treated with caution, since it was not determined at the position with highest amplitude, which is the resonance position.

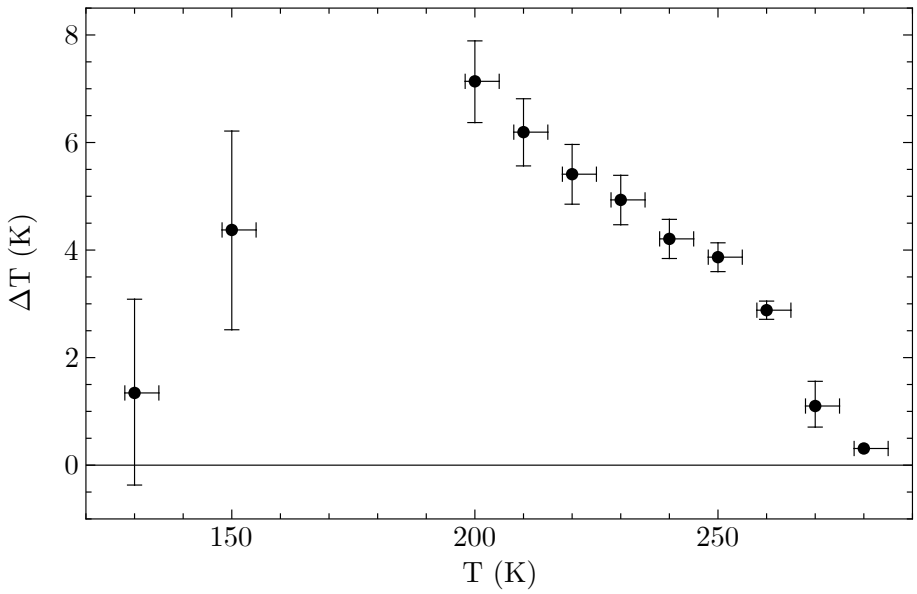

Figure 4.15.: Temperature dependent temperature difference between oop-direction 1 and oop-direction 2, whereas the x-axis denotes the temperature of oop-direction 1, while the temperature of oop-direction 2 would then be the same temperature plus the additional ΔT. When the errorbar of the plotted value is smaller than the pointsize it is not depicted.

4.4 Adapted Unidirectional Anisotropy Model

The results so far motivate the introduction of a new model for the free energy density of FeGe in FMR measurements. This time no unidirectional anisotropy is assumed, but a magnetization-dependent temperature, which in turn affects the magnetization. It is modeled by a temperature $\tilde{T}(\theta, \phi)$, which can lie between T and $T + \Delta T$. ΔT is the maximum change of temperature after inversion of the magnetic field. The general model can be written as

$$F = \underbrace{\frac{\mu_0}{2} \cdot \vec{M}\left(\tilde{T}(\theta,\phi)\right) \cdot \boldsymbol{N} \cdot \vec{M}\left(\tilde{T}(\theta,\phi)\right)}_{\text{shape anisotropy}} \quad \underbrace{- \vec{M}\left(\tilde{T}(\theta,\phi)\right) \cdot \vec{B}}_{\text{Zeeman term}}. \tag{4.5}$$

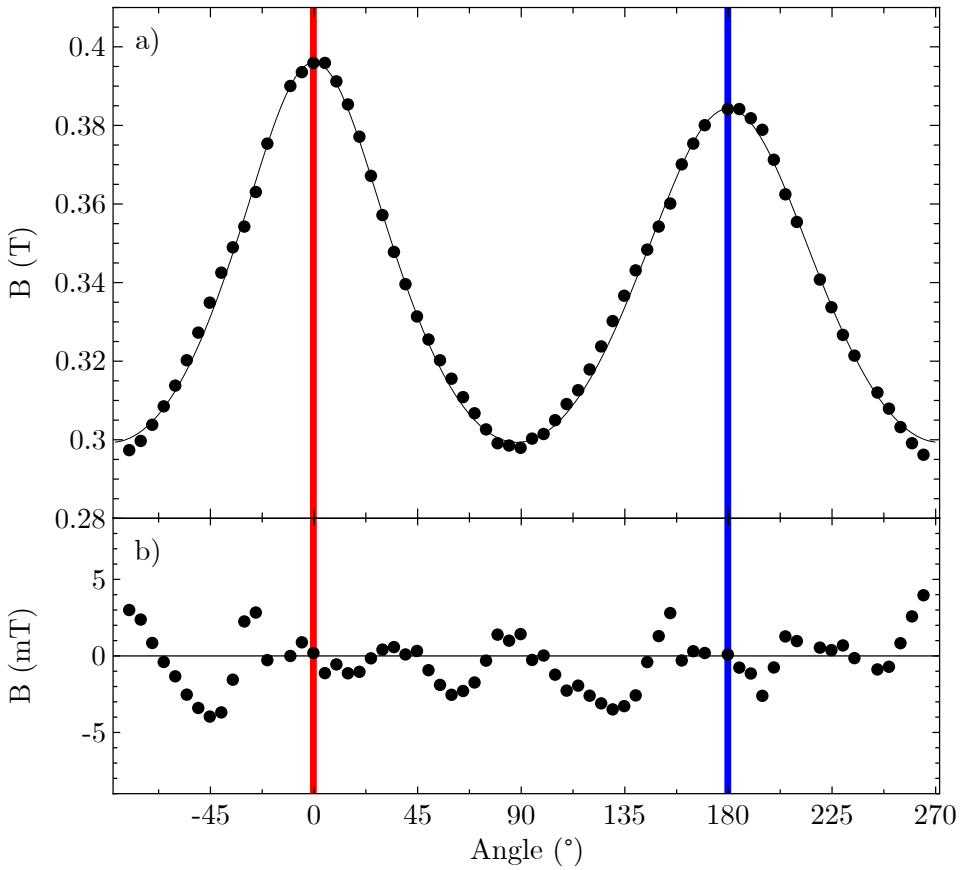

Figure 4.16.: a) comparison between the fitted temperature model and the measured zero crossings of the angular dependent FMR-measurement visible in Fig. 4.2. Only every fifth data point is depicted for clarity. b) field difference between the fitted model and the data points. In a perfect fit these points would be normally distributed around 0 T. The red and blue lines indicate the angles of the respective resonance spectra depicted in Fig. 4.3.

Here only the shape anisotropy and the Zeeman term are considered. When written in spherical coordinates and with a specific dependence of $\tilde{T}$ on T and ΔT this model becomes

$$\begin{aligned} F_S = n \cdot \frac{\mu_0}{2} \cdot M\left(\tilde{T}\left(\theta,\phi\right)\right)^2 \cos\left(2\theta\right) \\ - M\left(\tilde{T}\left(\theta,\phi\right)\right) B\left(\cos\left(\theta\right)\cos\left(\theta_B\right) + \cos\left(\phi-\phi_B\right)\sin\left(\theta\right)\sin\left(\theta_B\right)\right) \end{aligned} \tag{4.6}$$

$$\text{with} \quad \tilde{T}\left(\theta,\phi\right) = T + \frac{\Delta T}{2}\left(1-\cos\left(\theta\right)\right). \tag{4.7}$$

The highest difference in temperature happens with the magnetization along the z-direction ($\theta = 0°$ and $\theta = 180°$) of the coordinate system. How the dependence on the magnetization angles affects the calculation of the resonance position is described in Sec. A.2. Using this model for the angular dependent spectra (Fig. 4.2) the parameters in Tab. 4.2 were

obtained. The shift t due to the asymmetry of the lineshape and the demagnetization factor n were assumed again as fit parameters (see Sec. 4.1). The magnetization at the respective temperature was taken from the magnetization measurements at 350 mT seen in Fig. 4.8. The fit itself can be seen in Fig. 4.16. The biggest difference between the phenomenological

	Value	Error
ΔT	3.2 K	±0.6 K
n	0.40	±0.01
t	0.016 T	±0.001 T

Table 4.2.: Fit parameters (Fig. 4.16) of the angular dependent FMR measurement (Fig. 4.2) of the "L-shaped" FeGe sample (Fig. 4.9). The error was determined the same way as in Tab. 4.1.

fit in Fig. 4.4 and the temperature model is a better accordance between 90° and 270°. The magnetization change not only influences the height of the angular dependent resonance curve, but also its width through a change of the equilibrium position of the magnetization. This can't be modeled with the phenomenological unidirectional anisotropy. This model is better suited to describe the experimental results.

4.5 Ferromagnetic Resonance Lineshape

As mentioned in Sec. 4.3 the FMR lineshape of FeGe is distorted and in general does not represent the types of resonance lines discussed in Sec. 2.3.1. In this section this lines shape distortion is described in detail and several aspects, which could lead to such a distortion, are discussed.

4.5.1 Description of the FeGe Lineshape

At temperatures above 270 K the FMR lineshape is Dysonian (see Sec. 2.3.1). Here the sample volume in the cavity causes the asymmetry, as can be seen in Fig. 4.17, rather than the penetration depth itself, which is approximately 1 µm [70] for FeGe at X-band frequencies. This can occur, when the sample in resonance disturbs the microwave mode in the cavity. At temperatures below 270 K the lineshape becomes broader and starts to deviate from the Dysonian lineshape. Below 240 K resonances in the helical/conical phase (Sec. 3.2) start to appear in X-band FMR measurements and distort the lineshape even more. To separate the uniform mode and the helical/conical modes one has to conduct measurements at K-band or Q-band frequencies, where the helical/conical modes do not appear [73]. This has been done at various temperatures between 88 K and 290 K at K-band frequencies. For

the measurements a Bruker ER 6706KT cavity was placed inside an Oxford Instruments CF 935 helium cryostat for cooling. The cavity and the cryostat both have a temperature sensor, which were calibrated beforehand with a CX-SD temperature sensor at the sample position, thus leading to a temperature error of $\pm 2\,\mathrm{K}$, which is smaller than in the nitrogen X-band measurements (Sec. 4.3). The temperature is stabilized by a PID. A modulation frequency of 100 kHz was used with a modulation amplitude of $0.4 \times 10^{-3}\,\mathrm{T}$. The time constant was 5.12 ms with a conversion time of 10.24 ms and a microwave power of 1.975 mW. An FMR measurement at $T = 88\,\mathrm{K} \pm 2\,\mathrm{K}$ can be seen in Fig. 4.18. The external field points along oop-direction 1. Due to the strong asymmetry of the lineshape it is not possible to properly define a full width at half maximum. To still define a linewidth the peak-to-peak linewidth, that is the distance between maximum and minimum position in the derivative of the absorption spectrum, was used. In Fig. 4.18, these points are indicated by a blue and a yellow dot. The field difference between the inflection points is then the linewidth. For each measured temperature, the inflection points are plotted in Fig. 4.19 together with a grayscale contour plot of the FMR spectra. In the same figure the temperature dependent linewidth is plotted and compared with the temperature dependent magnetization with an external magnetic field of 850 mT pointing along the oop-direction. The resemblance of the temperature dependence of the magnetization and the temperature dependence of the linewidth is no typical result for FMR measurements. From the intrinsic linewidth seen in Eq. 2.16 one would suggest a reciprocal dependence on the magnetization. The following interpretation of the linewidth is based on the assumption that a distribution of resonance lines is visible rather than a single very broad line. This assumption rests on the strong deviation of the resonance line from a Lorentzian or Dysonian lineshape. The inflection points marked in fig. 4.19 can then be viewed as the borders of the resonance line distribution.
A distribution in general can have different origins: a) a polycrystallinity of the sample. This explanation can only be a minor contribution as shown in Sec. 4.5.2 by a detailed theoretical analysis of the distribution, which would follow from the magnetocrystalline anisotropy in FeGe. b) a temperature gradient in the sample. This, however, can not explain the temperature dependent behavior of the linewidth. Along the hard axis it is expected, that with lower temperature and therefore higher magnetization the resonance line moves to higher fields. It is not possible, that the resonance distribution spreads to lower fields at lower temperatures, which is, however, the case. c) A inhomogenous demagnetization field inside the sample. The calculation of demagnetization fields in different geometries is a standard problem. It is known that the local demagnetization field can vary strongly dependent on the position inside samples with non-ellipsoidal shape [39]. This causes an inhomogeneous line broadening and can cause complex FMR lineshapes [88]. Haraldson and Smith [72] already used this argument to explain certain features in the FeGe lineshape, which they called edge modes. The skin depth of FeGe further adds to this, since the edge regions typically contribute the most to varieties in the demagnetization field.

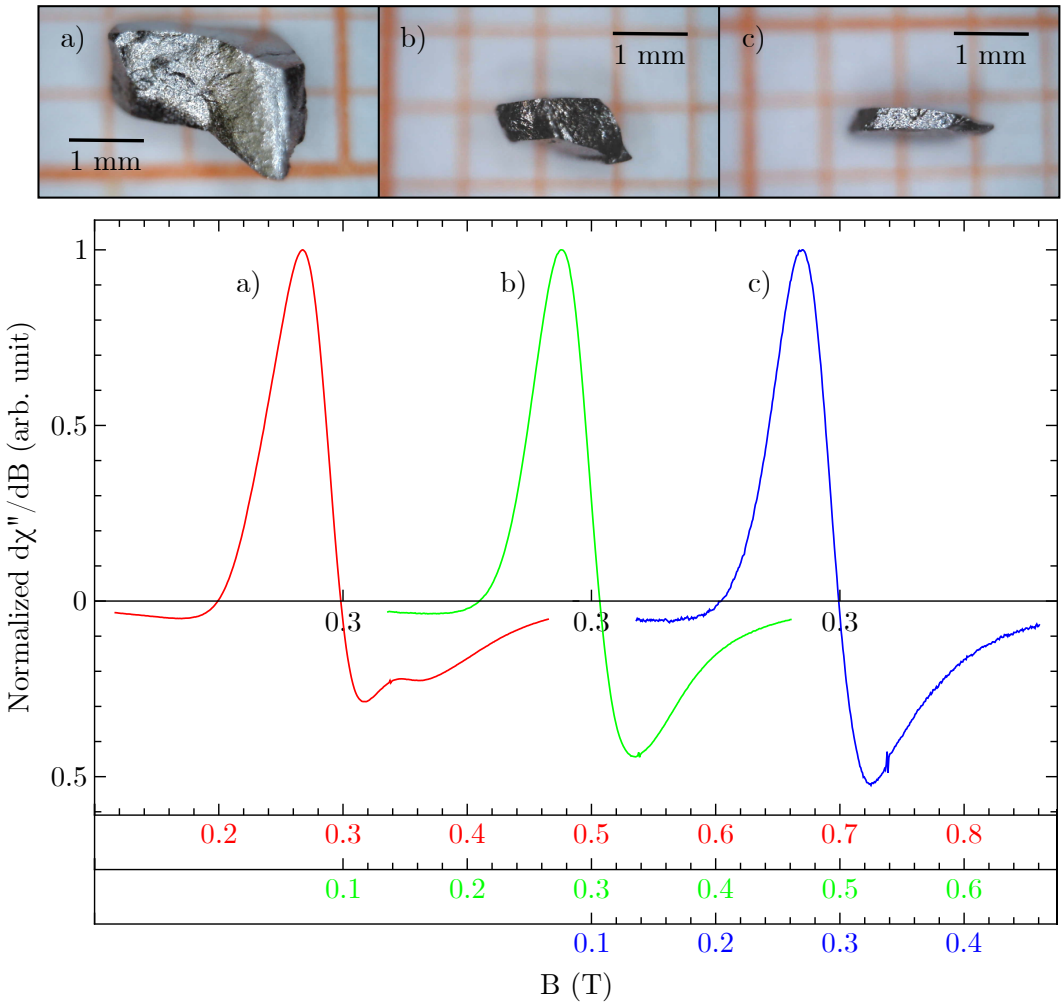

Figure 4.17.: Asymmetry of the Dysonian lineshape at a temperature of $T = 275\,\mathrm{K} \pm \frac{5\,\mathrm{K}}{2\,\mathrm{K}}$ for different sample sizes together with a photo of the respective sample. The frequencies were a) $f = 9.469\,\mathrm{GHz} \pm 0.001\,\mathrm{GHz}$ b) $f = 9.469\,\mathrm{GHz} \pm 0.001\,\mathrm{GHz}$ c) $f = 9.470\,\mathrm{GHz} \pm 0.001\,\mathrm{GHz}$. For better comparison the resonance lines b) and c) were shifted by 0.2 mT and 0.4 mT respectively. All resonance lines were normalized. The volumes of each sample were calculated using the measured weight and the density of FeGe: a) $V = 2.07\,\mathrm{mm}^3 \pm 0.06\,\mathrm{mm}^3$, b) $V = 0.84\,\mathrm{mm}^3 \pm 0.01\,\mathrm{mm}^3$ and c) $V = 0.51\,\mathrm{mm}^3 \pm 0.06\,\mathrm{mm}^3$.

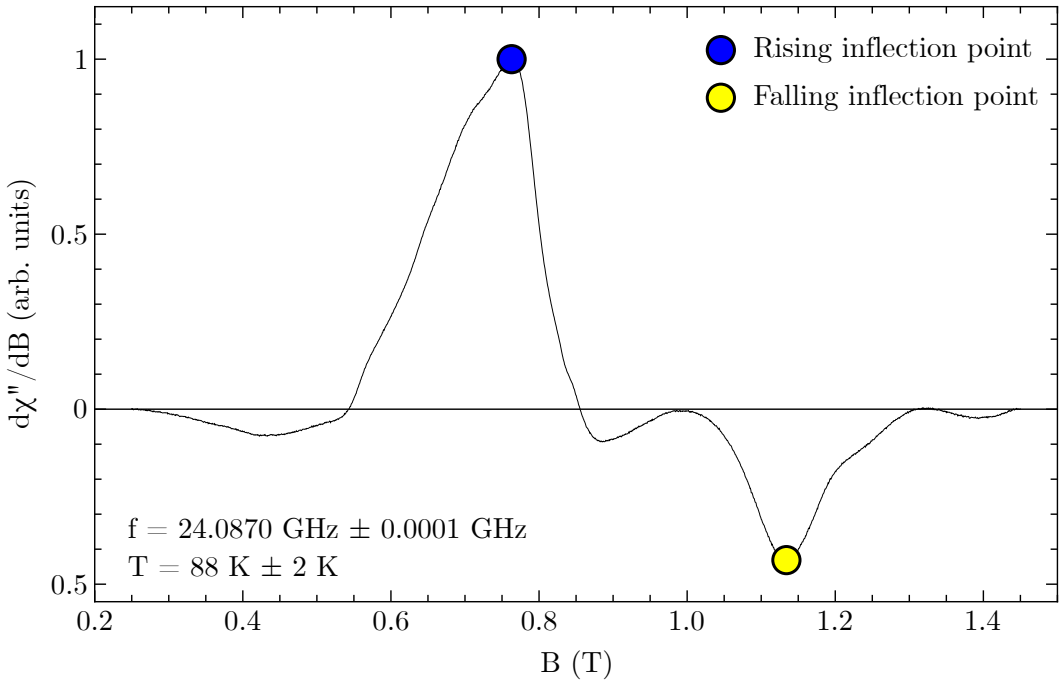

Figure 4.18.: Resonance spectrum at $T = 88.2\,\mathrm{K} \pm 0.5\,\mathrm{K}$. The external magnetic field points along oop-direction 1. The frequency was $f = 24.0870\,\mathrm{GHz} \pm 0.0001\,\mathrm{GHz}$. The blue and yellow point indicate a local amplitude maximum and minimum respectively and indicate the inflection points of the resonance line.

In the following two demagnetization tensors are chosen and the related temperature dependent resonance position calculated. The two tensors represent the easiest and hardest directions possible by shape anisotropy. It is checked, whether the resonance line distribution is within these borders. To further simplify this calculation, it is assumed that all magnetic moments in the sample are aligned along the principal direction of an ellipsoid. The demagnetization tensor from Eq. 2.8 in such a case can be written in a diagonal form [29, p. 129]:

$$\boldsymbol{N} = \begin{pmatrix} N_{xx} & 0 & 0 \\ 0 & N_{yy} & 0 \\ 0 & 0 & N_{zz} \end{pmatrix}. \tag{4.8}$$

The influence of the demagnetization field on the resonance position is calculated using Eq. 2.15 and the free energy density

$$F = \underbrace{\frac{\mu_0}{2} \cdot \vec{M} \cdot \boldsymbol{N} \cdot \vec{M}}_{\text{shape anisotropy}} \quad \underbrace{- \vec{M} \cdot \vec{B}}_{\text{Zeeman term}} . \tag{4.9}$$

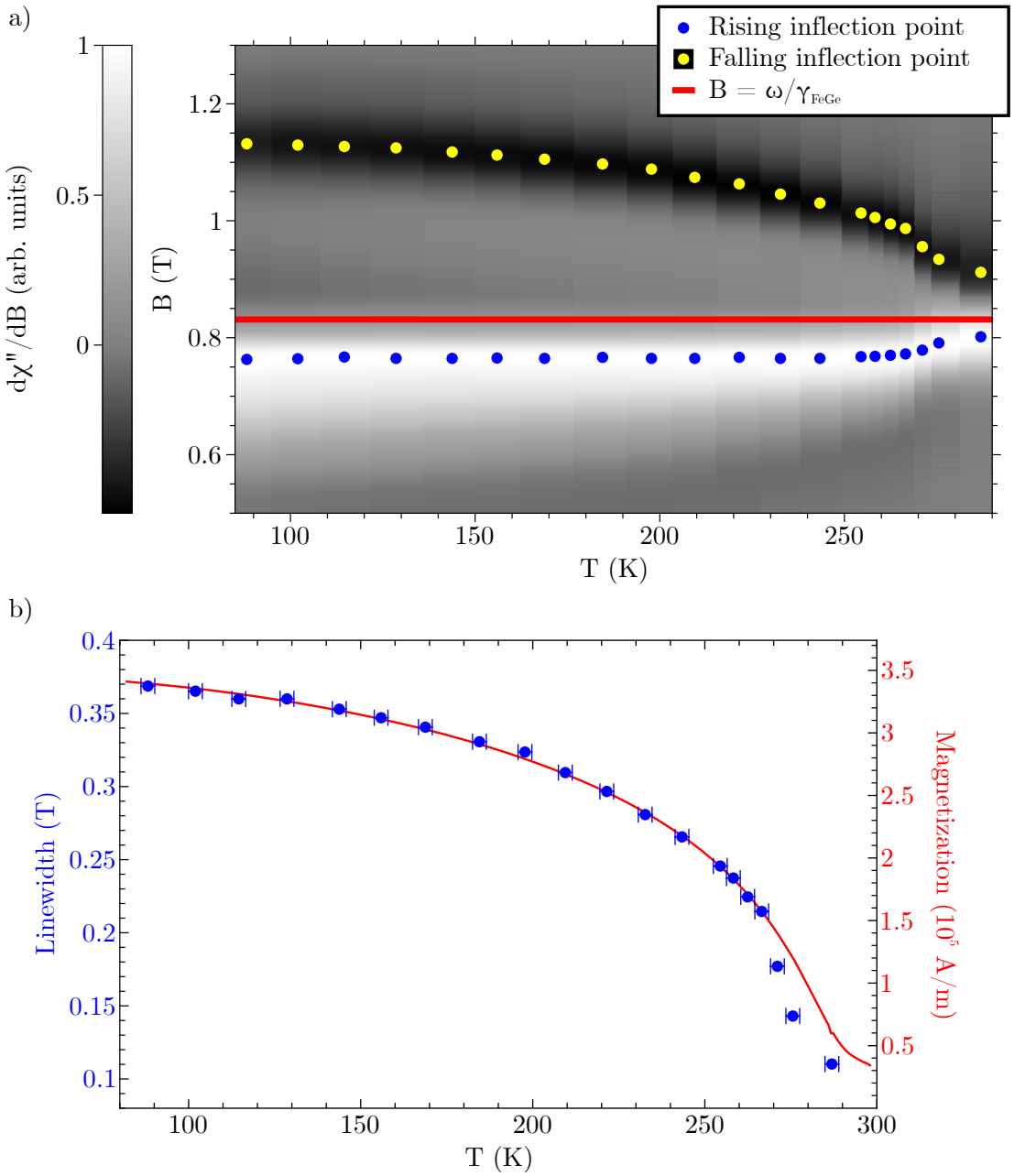

Figure 4.19.: a) FMR spectra as a grayscale contour plot dependent on the external magnetic field and the temperature for oop-direction 1. All frequencies of the spectra lay in an interval of 12 MHz around 24.083 GHz. The yellow and blue dots represent the respective local minimum and local maximum position of each spectrum as indicated in Fig. 4.18. The red curve is the expected resonance position of FeGe without any anisotropy. b) The temperature dependent peak-to-peak linewidth of each spectrum in a) compared with the temperature dependent magnetization at 850 mT along the oop-direction shown in Fig. 4.8.

It contains only the Zeeman term and the shape anisotropy. The calculation is done as described in Sec. 4.1. The only difference is that there is no resonance field, which can be used for the minimization of the free energy density to calculate the equilibrium position of the magnetization. Therefore a start field is needed, which lies above the assumed resonance field. The direction of magnetization is then calculated and used to determine the respective resonance field, which in turn is used again to calculate the magnetization direction. This cycle is repeated until self-consistency is achieved, which is numerically implemented through an upper bound of the difference between two consecutive calculated resonance fields. This calculation was done w.l.o.g. along the z-axis using the demagnetization tensors $N_{xx,1} = 0$, $N_{yy,1} = 0$ and $N_{zz,1} = 1$ and $N_{xx,2} = 1$, $N_{yy,21} = 0$ and $N_{zz,2} = 0$. These two represent the hardest and easiest direction of shape anisotropy along the z-direction. Furthermore the temperature dependent magnetization measured at 850 mT shown in Fig. 4.8 was used as the fixed magnetization in this calculation. The results can be seen in Fig. 4.20. The resonance

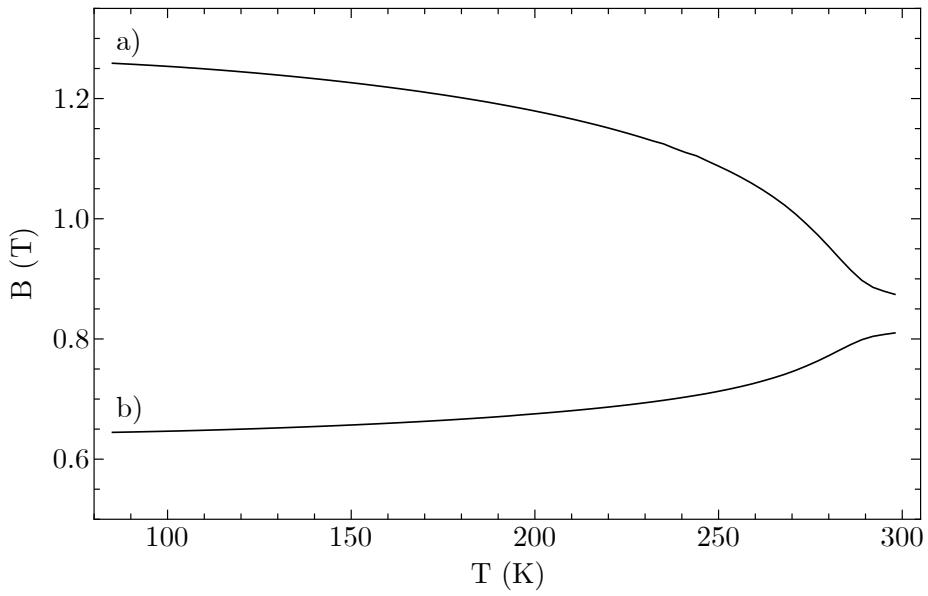

Figure 4.20.: Temperature dependent resonance field position calculated using Eq. 2.15 and Eq. 4.9 with the external magnetic field pointing along the z-direction. The respective demagnetization tensors were a) $N_{xx,1} = 0$, $N_{yy,1} = 0$ and $N_{zz,1} = 1$ and b) $N_{xx,2} = 1$, $N_{yy,21} = 0$ and $N_{zz,2} = 0$. A g-factor for FeGe of 2.07 [73] was assumed together with a frequency of 24.083 GHz.

positions display the same temperature dependent behavior as the measured inflection points in Fig. 4.19 a). At the same time these inflection points lie within the limits set by shape anisotropy in Fig. 4.20. This shows that the behavior of the FeGe FMR linewidth can be explained with inhomogeneous demagnetization fields.

Another important aspect of FMR is its intensity, which is the area below the resonance curve. It can be determined through double integration of the respective FMR spectrum. Due to the asymmetry of the resonance line the limits of integration have to be chosen consistently at each temperature to make the intensity comparable. In this case the inflection points were used as the limits. The results can be seen in Fig. 4.21. The intensity follows as expected the temperature dependent behavior of the magnetization as in Fig. 4.8. The sharp rise around 260 K could be caused by fluctuations of the order parameter in the vicinity of a magnetic phase transition [89].

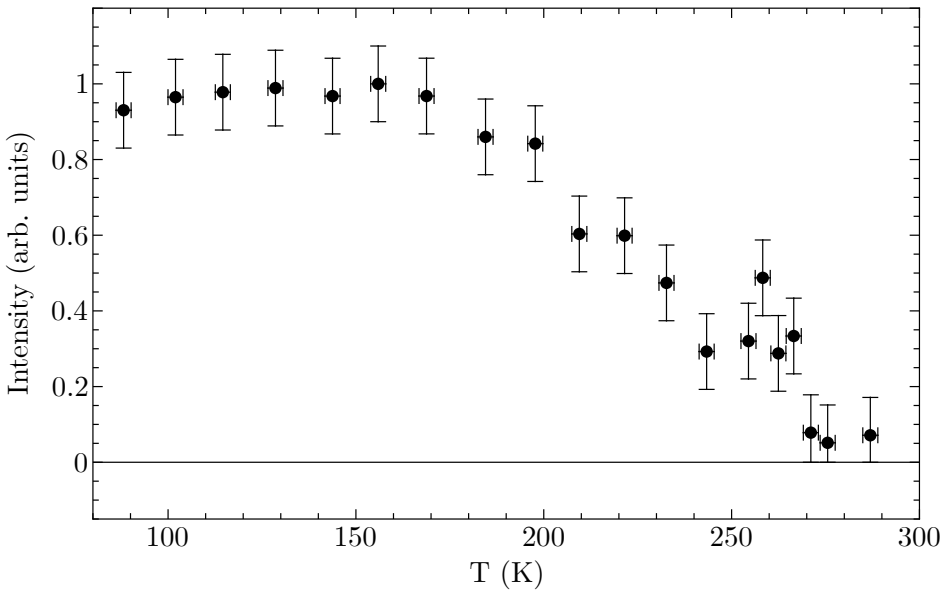

Figure 4.21.: Temperature dependent FMR resonance line intensity of the FMR measurement depicted in Fig. 4.19. The intensity was obtained trough double numerical integration of the FMR spectra.

4.5.2 Modeling the Ferromagnetic Resonance Spectra of a Polycrystal

A polycrystalline material consists of a finite number of single crystals. These are either randomly oriented or textured in a way that preferred orientations exist within the sample. The simplest way to model the magnetic response of a polycrystalline material is to assume that every crystalline direction is equally abundant. The idea is, to calculate the resonance field for each crystalline direction. This is approximated by a finite but sufficient number of sample directions. This approach implies non-interacting grains [21, p. 54], which was suggested by VanVleck [90]. When these grains form a different geometry than a sphere together, the

demagnetization field has to be taken into consideration. The methods for these calculations are collectively presented in Sec. A.3. With them one is able to compute a distribution of resonance lines of a polycrystalline material with and without shape anisotropy. Here only the results are discussed. To determine whether the broadening of the resonance line at low temperatures (Fig. 4.18 and Fig. 4.19) can be explained with the polycrystallinity of the sample, the resonance distributions were calculated at a frequency of 24 GHz and a temperature of 88 K. A magnetization $M = 3.4 \times 10^5\,\mathrm{A\,m^{-1}}$, determined by VSM measurements, was assumed. The magnetocrystalline anisotropy constants of $K_4\,(88\,\mathrm{K}) = -3250\,\mathrm{J\,m^{-3}}$ and $K_6\,(88\,\mathrm{K}) = 6500\,\mathrm{J\,m^{-3}}$ were taken from [8]. Additionally a g-factor for FeGe of 2.07 [73] was assumed. The results can be seen in Fig. 4.22 with and without the shape anisotropy, which was calculated with Eq. 4.2 and an aspect ratio $\tau = 1/3$ taken from Fig. 4.9. In the former case only the distributions along the easy and the hard direction are shown. The FeGe line broadening through the polycrystallinity is approximately 30 mT, while the line broadening in Fig. 4.19 is as high as 350 mT. One can conclude that the broadening of the line cannot be explained through the polycrystallinity. Another proof is that this line broadening is also visible in measurements with single crystalline samples [71].

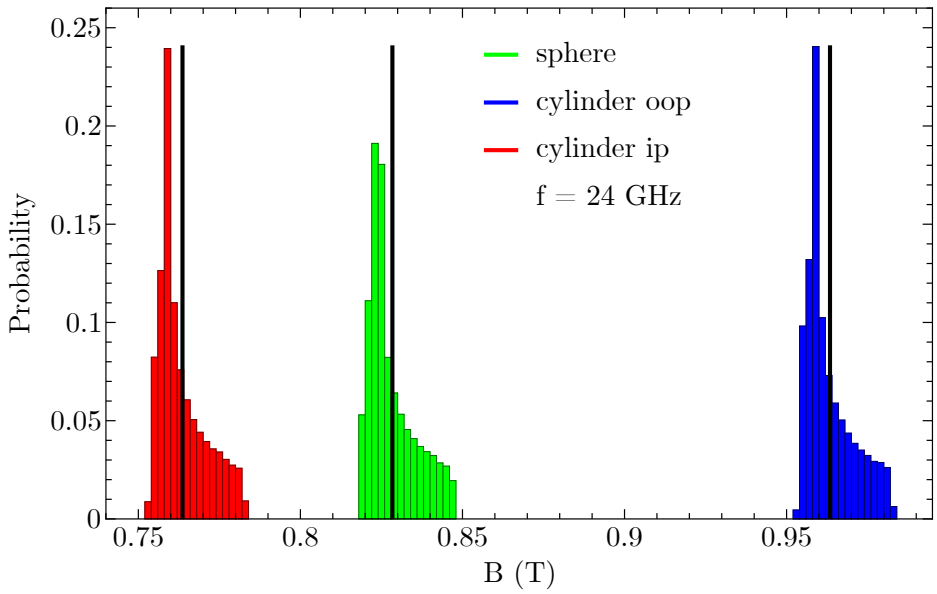

Figure 4.22.: Histogram of the probability for resonance positions, when the crystallographic direction is randomly oriented. The green histogram is calculated with just the magneto-crystalline anisotropy of Eq. 3.1 with $K_4\,(88\,\mathrm{K}) = -3250\,\mathrm{J\,m^{-3}}$ and $K_6\,(88\,\mathrm{K}) = 6500\,\mathrm{J\,m^{-3}}$ taken from [8] a g-factor for FeGe of 2.07 [73] and a rounded measured magnetization of $340\,000\,\mathrm{A\,m^{-1}}$ at 88 K. The red and blue histograms are the respective easy and hard direction of a cylinder with an aspect ratio of $\tau = 1/3$. The black line represents the resonance position without any magnetocrystalline anisotropy.

5 Magnon-Scattering Model for FeGe

In Sec. 4.3.1 a temperature model based on changes of the magnetization was used to describe and quantify the unidirectional anisotropy. Here, the origin of the different temperatures due to the magnetization is discussed on the basis of unidirectional dynamic magnetic excitations in FeGe, which were introduced in Sec. 2.2.1 as spin-waves or magnons.

5.1 Dispersion Relation with and without DMI

The dispersion relation is the frequency (or energy) of a wave as a function of the wave vector $\vec{k} = (k_x, k_y, k_z)$. It can be derived through the high-frequency magnetic susceptibility tensor in the same way as the position of FMR [13], which is, in fact, just a special case ($\vec{k} = 0$) of the spin-wave dispersion. Assuming a spherical isotropic ferromagnet the magnetic free energy density is the sum of the Zeeman term in Eq. 2.6 and the exchange term in Eq. 2.5 [21, p. 179f.] and can be written as

$$\mathrm{F_{EX}} = \frac{A}{2M^2}\nabla^2\vec{M} - \vec{M}\cdot\vec{B}_{\mathrm{ext}}. \tag{5.1}$$

A is the exchange stiffness (Sec. 2.2.1). By solving the Landau-Lifshitz-Gilbert equation (Eq. 2.9) with the modified Ansatz of Eq. 2.10 and using the functional derivative Eq. 2.3 of Eq. 5.1 to determine the effective field one can calculate the high-frequency magnetic susceptibility tensor $\boldsymbol{\chi}$ (Eq. 2.11) with the formalism developed by Benjamin Zingsem [47]. The modified version of the Ansatz has the form

$$\begin{aligned} \vec{B} = \vec{B}_0 + \vec{b} = \vec{B}_0 + \vec{b}_0 \mathrm{e}^{i\left(k_x x + k_y y + k_z z - \left(\omega t + \frac{\pi}{2}\right)\right)} \\ \text{and} \quad \vec{M} = \vec{M}_0 + \vec{m} = \vec{M}_0 + \vec{m}_0 \mathrm{e}^{i(k_x x + k_y y + k_z z - \omega t).} \end{aligned} \tag{5.2}$$

Additionally, the three-dimensional Jacobian matrix $\mathfrak{J}_{\vec{r}}$ has to be introduced, which is defined as

$$\mathfrak{J}_{\vec{\xi}}\left(\vec{f}\left(\vec{\xi}\right)\right) = \begin{pmatrix} \frac{\partial f_1}{\partial \xi_1} & \frac{\partial f_1}{\partial \xi_2} & \frac{\partial f_1}{\partial \xi_3} \\ \frac{\partial f_2}{\partial \xi_1} & \frac{\partial f_2}{\partial \xi_2} & \frac{\partial f_2}{\partial \xi_3} \\ \frac{\partial f_3}{\partial \xi_1} & \frac{\partial f_3}{\partial \xi_2} & \frac{\partial f_3}{\partial \xi_3} \end{pmatrix}. \tag{5.3}$$

In this case $\vec{f}(\vec{\xi})$ denotes an arbitrary three-dimensional vector function dependent on the parameter vector $(\xi_1, \xi_2, \xi_3)^{\mathrm{T}}$. The Jacobian matrix is then the matrix of all first-order derivatives of the vector function with respect to the parameter vector. Additionally, the

Landau-Lifshitz-Gilbert equation must be written in the form

$$L\left(\vec{b},\,\vec{m}\right) = \frac{\partial \vec{M}}{\partial t} + \gamma \vec{M} \times \vec{B}_{\text{eff}} - \frac{\alpha}{M}\vec{M} \times \frac{\partial \vec{M}}{\partial t} = 0, \tag{5.4}$$

which describes a hyper-surface dependent on the small oscillating perturbations $\vec{b}$ and $\vec{m}$ in the Ansatz. According to Benjamin Zingsem [47] the high-frequency magnetic susceptibility tensor can be written as

$$\boldsymbol{\chi} = -\left(\left(\mathfrak{J}_{(m_x,\,m_y,\,m_z)^{\mathrm{T}}}\left(L\left(\vec{b},\,\vec{m}\right)\right)\Big|_{\vec{m}=0,\,\vec{b}=0}\right)^{-1} \mathfrak{J}_{(b_x,\,b_y,\,b_z)^{\mathrm{T}}}\left(L\left(\vec{b},\,\vec{m}\right)\right)\Big|_{\vec{m}=0,\,\vec{b}=0}\right). \tag{5.5}$$

As shown in Eq. 2.12 only the first row and first column element of the high-frequency susceptibility tensor χ_{11} is needed for the calculation of the dispersion. For the free energy density in Eq. 5.1 and w.l.o.g. an external field pointing in the z-direction, the determined formula for χ_{11} is

$$\lim_{\alpha\to 0} \operatorname{Im}\left(\chi_{11}\right) = -\frac{M^2\gamma^2\left(B_z M + A\left(k_x^2 + k_y^2 + k_z^2\right)\right)}{\gamma^2\left(B_z M + A\left(k_x^2 + k_y^2 + k_z^2\right)\right)^2 - M^2\omega^2} \tag{5.6}$$

As discussed in Sec. 4.1 the parameter α is assumed to be 0 also here. The resonance frequency is now the singularity of Eq. 5.6, i.e. the frequency ω where the denominator is zero. The final dispersion relation for an isotropic ferromagnet is then

$$\omega = \frac{\gamma}{M}\left(B_z M + A\left(k_x^2 + k_y^2 + k_z^2\right)\right) \tag{5.7}$$

At $\vec{k} = 0$ it has the typical relationship $\omega = \gamma B$ for the FMR position without anisotropy [20, p. 3]. Additionally, it has a term proportional to the wave vector components squared, which is a well known result for the dispersion [91, p. 60], and has the form of a parabola with its vertex at the position of FMR. This quadratic relationship is only valid for small values of (k_x, k_y, k_z). To calculate the influence of the DMI to the dispersion relation the DMI free energy density term in Eq. 2.5 has to be added to Eq. 5.1, which leads to

$$\mathrm{F}_{\mathrm{DMI}} = \frac{A}{2M^2}\nabla^2\vec{M} - \vec{M}\cdot\vec{B}_{\text{ext}} + \frac{d}{M^2}\vec{M}\left(\nabla \times \vec{M}\right). \tag{5.8}$$

When the dispersion is calculated the same way as the one without DMI, one obtains

$$\omega = \frac{\gamma}{M}\left(B_z M + A\left(k_x^2 + k_y^2 + k_z^2\right) + 2dk_z\right). \tag{5.9}$$

The DMI adds an additional term to the dispersion, which is proportional to k_z [13]. This describes a non-reciprocity of spin-waves, meaning that spin-waves traveling with the same

wave length in opposite directions oscillate with different frequencies. This asymmetry in the spin-wave spectrum exists only for components of the wave vector along the effective magnetic field. A plot of this dispersion can be seen in Fig. 5.1.

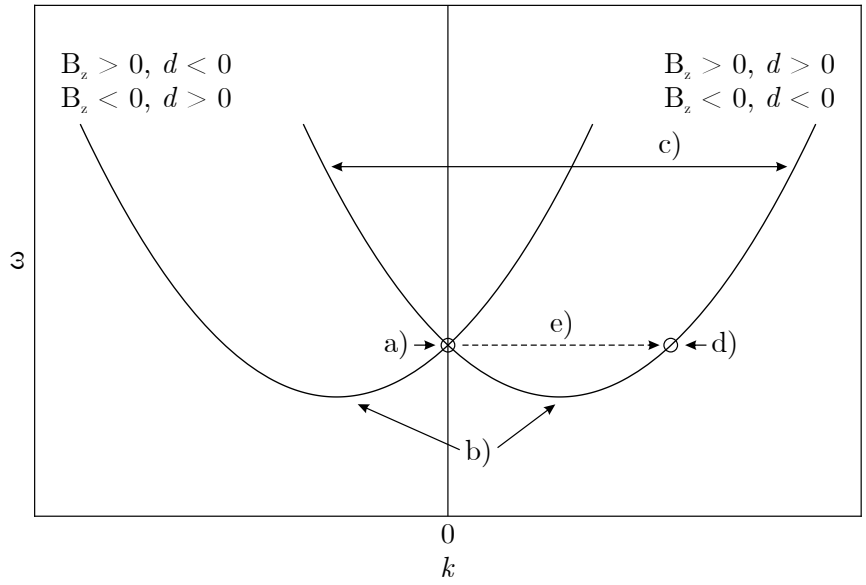

Figure 5.1.: Dispersion relation $\omega(k)$ with DMI (Eq. 5.8) plotted for different signs of B_z and d. a) is the new uniform mode with DMI b) is the uniform mode without DMI. c) is a standing spin wave mode, which can be excited in FMR in confined geometry. d) is a traveling spin wave mode, which is excited by magnon-magnon-scattering (see e)) of the uniform spin wave mode.

5.2 Heat Capacity of Magnons in FeGe

The specific heat capacity is the amount of heat necessary to increase the temperature of one cubic meter of the investigated material by one Kelvin. It is denoted by c_V. The specific heat capacity has different contributions, for example vibrational, electronic or magnetic. Here, the magnetic contribution to the specific heat capacity of FeGe is calculated based on [92]. This calculation provides the amount of energy necessary to heat up the sample to the reported temperature differences (Fig. 4.15), with the simplified assumption that only the magnonic system changes its temperature. That means neither magnon-phonon-scattering nor thermal conduction is taken into account. A comparison with the microwave power then unveils whether it is sufficient for such a temperature change. This calculation does not include any considerations about the cause of such an asymmetry of the temperature. It only provides information about the energy needed. The specific heat is given by

$$c_V = \frac{\partial U}{\partial T}, \tag{5.10}$$

which is the derivative of the inner energy U with respect to the temperature T [93, p. 276]. The inner energy of the magnonic system must be calculated with Bose–Einstein statistics as

$$U_{\mathrm{mag}} = \frac{1}{(2\pi)^3} \int_0^{k_m} \mathrm{d}^3k \quad \underbrace{\hbar\omega(\vec{k})}_{\text{energy}} \quad \underbrace{\frac{1}{\mathrm{e}^{\hbar\omega(\vec{k})/k_BT}}}_{\text{occupation number}} \tag{5.11}$$

$$\text{with} \quad k_m = \kappa \frac{\sqrt[3]{6\pi^2}}{a}. \tag{5.12}$$

For that the occupation number of a magnon state is multiplied with the respective energy and integrated over the Brillouin zone, which contains all information about all possible waves. Equation 5.12 is the edge of the Brillouin zone with the lattice constant a and the scaling factor κ [94]. Since no scaling factor for FeGe is given in literature, I assume for simplicity $\kappa = 1$. The magnetic part of the specific heat $c_{V\mathrm{mag}}$ is the derivative of Eq. 5.11 with respect to T:

$$c_{V\mathrm{mag}} = \frac{\partial U_{\mathrm{mag}}}{\partial T} = \frac{1}{(2\pi)^3} \int_0^{k_m} \mathrm{d}^3k \frac{\left(\hbar\omega(\vec{k})\right)^2}{k_BT^2} \frac{\mathrm{e}^{\hbar\omega(\vec{k})/k_BT}}{\left(\mathrm{e}^{\hbar\omega(\vec{k})/k_BT} - 1\right)}. \tag{5.13}$$

With this formula the specific heat can be calculated using the dispersion (Eq. 5.9) with the values $A = 1.37 \times 10^{-12}\,\mathrm{J\,m^{-1}} \pm 0.13 \times 10^{-12}\,\mathrm{J\,m^{-1}}$ for the exchange stiffness and $d = 2.48 \times 10^{-4}\,\mathrm{J\,m^{-2}} \pm 0.26 \times 10^{-4}\,\mathrm{J\,m^{-2}}$ for the DMI constant both given in [75] and a lattice parameter of $a = 4.700\,\text{Å} \pm 0.002\,\text{Å}$ [27, 28]. The calculated magnetic part of the specific heat is shown in Fig. 5.2. The energy necessary to heat a certain volume V of FeGe by $\Delta T = T_2 - T_1$ is given by

$$E_{\Delta T} = V \int_{T_1}^{T_2} \mathrm{d}T\, c_{V\mathrm{mag}}. \tag{5.14}$$

For the biggest temperature difference in Fig. 4.15 of $\Delta T = 7.1\,\mathrm{K} \pm 0.8\,\mathrm{K}$ at a temperature of $T = 200\,\mathrm{K} \pm {}^{5\,\mathrm{K}}_{2\,\mathrm{K}}$ and with a volume of $\mathrm{V} = 0.84\,\mathrm{mm}^3 \pm 0.01\,\mathrm{mm}^3$ the energy evaluates to $E_{\Delta T} = 1.12\,\mathrm{mJ} \pm 0.14\,\mathrm{mJ}$. The experiment was performed with a microwave power of $P = 1.975\,\mathrm{mJ\,s^{-1}}$, which is a sufficient amount to change the temperature of the whole sample. Additionally, due to the penetration depth of the microwave, only the surface region needs to be heated. Furthermore, the dispersion relation in Eq. 5.9 is only valid for small k and otherwise overestimates the needed energy. The obtained value of $E_{\Delta T}$ is therefore an upper limit.

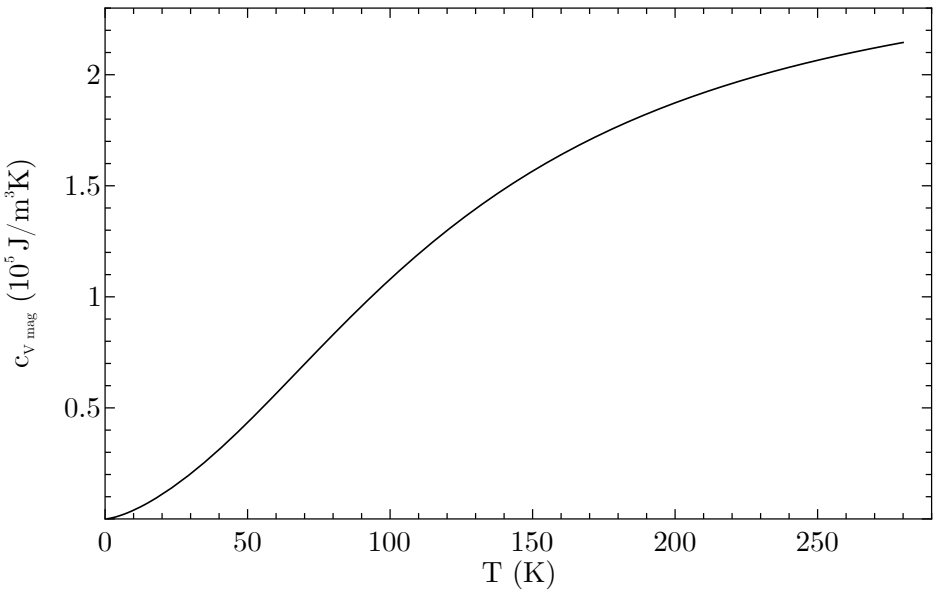

Figure 5.2.: Temperature dependent magnetic part of the specific heat $c_{V\mathrm{mag}}$ of FeGe calculated according to Eq. 5.13. The parameters and references are mentioned in the text.

5.3 Geometry Dependent Heating by Magnon-Scattering

In general, the decrease in magnitude of the magnetization M is related to the number of magnons, which are excited in the sample:

$$M = \left(1 - N^{-1} \sum_k n\left(k\right)\right) M\left(T = 0\right). \tag{5.15}$$

More excited magnons mean less magnetization [92, 94]. Here, $M\left(T = 0\right)$ is the magnetization at 0 K and M after the excitation of $\sum_k n\left(k\right)$ magnons. N is the total number of spins in the sample. Each excited magnon lowers the magnetization. The number of thermally induced magnons is given again by Bose–Einstein statistics [92] and leads to a temperature dependence of the magnetization of

$$M\left(T\right) = \left(1 - \frac{a^3}{2\pi^2} \int_0^{k_m} \mathrm{d}^3k \frac{1}{\mathrm{e}^{\hbar\omega(\vec{k})/k_B T} - 1}\right) M\left(0\right). \tag{5.16}$$

Here, a is the lattice parameter. However, the calculation of the amount of magnons additionally excited by the microwave is complex. Detailed information about the magnetic system and the electromagnetic wave at the sample position is necessary [20, p. 4].
During FMR measurements the magnetic system is in a steady state of nonequilibrium [21, p 283]. On the one hand the driving microwave field continuously excites magnons, while on the other hand relaxation processes dissipate energy. In the state of nonequilibrium the temperature difference postulated in Sec. 4.3 can be explained in two ways. Either the whole sample changes its temperature or just the magnonic system. In the former case a temperature sensor placed on the sample would detect a temperature change after inversion of the magnetic field during microwave excitation. In the latter case only a change of the static magnetization would be detected, for example in a VSM measurements. Until now, relaxation processes were described by the phenomenological damping parameter α introduced in Sec. 2.3. In one way or another these relaxation processes dissipate their energy into the phononbath, i.e. heat. This can either happen directly or through intermediate spin-wave states [91, p 95]. The basic idea of the magnetization-dependent temperature is that these intermediate spin-wave states, due to the asymmetric dispersion visible in Fig. 5.1, contain an asymmetric distribution of wave vectors $\vec{k}$. In what follows, the connection between this asymmetric distribution of wave vectors and the proposed temperature difference between opposite magnetic field directions is explained. Exemplary, this is done on the basis of two-magnon scattering. Two-magnon-scattering describes a direct transfer of energy from one magnon to another [21, p. 300]. In FMR-measurements the main two-magnon-process is the scattering of the uniform mode ($k = 0$), due to the steady state excitation of this mode by the microwave field. Due to the conservation of energy the excited modes have to be on the same energy level as the uniform mode [21, p. 302]. Such a two-magnon-process is depicted in Fig. 5.1 e). For opposite magnetic field directions the wavevector k of this excited mode is inverted. The consequences of this are shown in Fig. 5.3. In b) one edge of a schematic FeGe sample is shown. The part of the sample, which is penetrated by the microwaves (around 1 µm penetration), is marked gray and on one side confined by a rough surface. Only this part of the sample is of interest in an FMR measurement. The DMI constant d is now chosen in such a way, that the wavevector of the, through the two-magnon-process, excited magnon points in the direction of the magnetic field. Two opposite magnetic field directions are compared, where the magnetic field either points towards (a) & b)) or away (c) & d)) from the rough surface. Similarly the excited magnons either travel towards or away from the surface. The idea is now that when the magnons are traveling towards the surface, they participate in magnon-phonon scattering, which ultimately increases the temperature of the surface. However, when The magnons are traveling away from the surface, they will participate in magnon-phonon scattering inside the sample. Due to steady contact of the surface with the thermal bath a temperature difference between opposite magnetic field directions during dynamic excitation occurs.

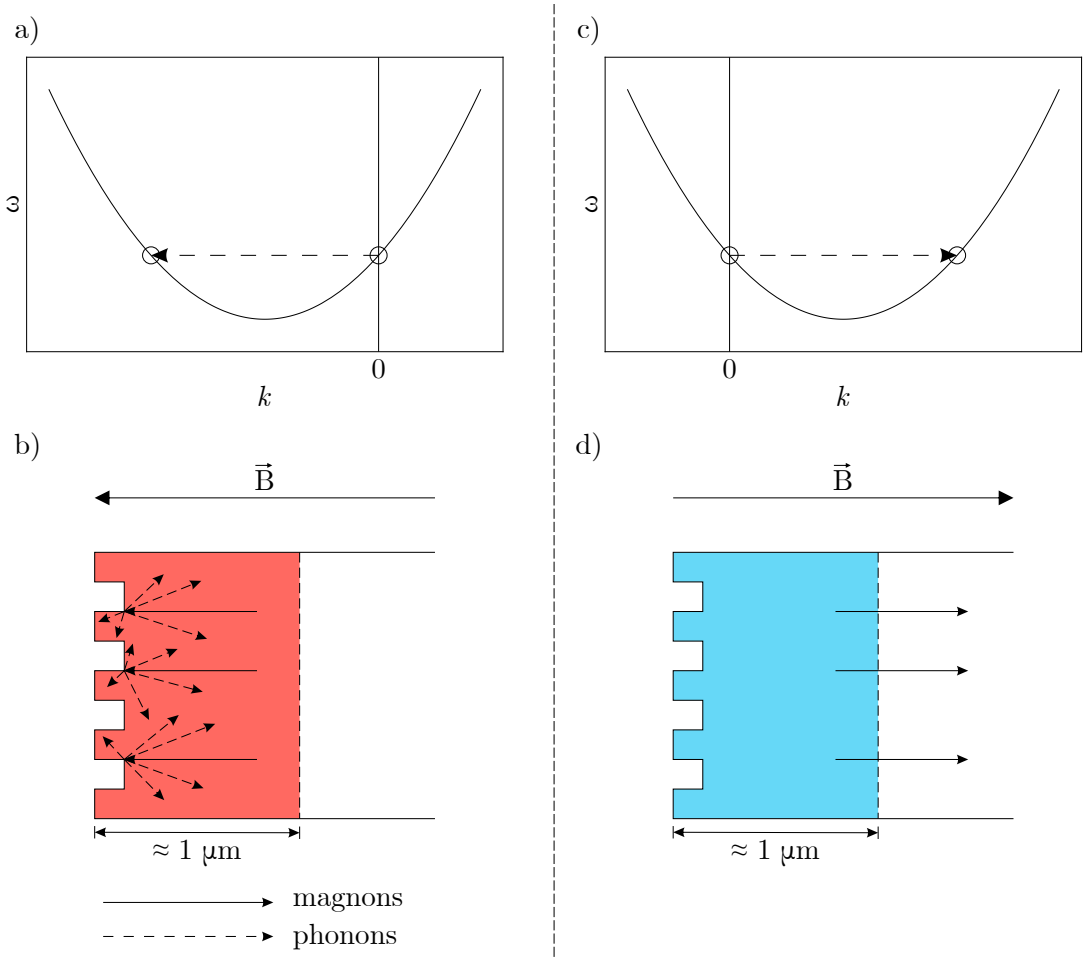

Figure 5.3.: Schematic illustration of the magnetization-dependent temperature model. b) is a depiction of one side of the sample. The gray area marks the penetration depth of the microwaves in an FMR experiment. The left edge of the sample consists of a rough surface, while anything beyond the penetration depth is not depicted. An arrow above the sample indicates the direction of the external magnetic field. a) depicts the magnon dispersion relation of this configuration. The wave number corresponds to magnons parallel to the external magnetic field. A dashed arrow indicates the 0-k process exciting traveling magnons as described in the text. These magnons are illustrated in b) as a solid arrow inside the sample. They are traveling towards the rough surface and scattered as phonons (dashed arrow). c) and d) illustrate the same situation as a) and b), but with an opposite magnetic field direction. This mirrors the dispersion curve about the ω axis, resulting in an inverted direction of the excited magnons, which are then traveling away from the surface.

5.3.1 Limits of the Heating Model

Here, details and arguments against the model introduced in Sec. 5.3 of magnetization-dependent temperature are discussed.
First of all, the proposed model discusses only one side of the FeGe sample. The opposite side should display the same behavior, but with an opposite dynamic unidirectional anisotropy. It can be argued, that an asymmetry between both surfaces exists like a different size, roughness or composition. To check whether such a geometric asymmetry can explain the results, two surfaces with defined roughness have to be created on an otherwise ideal FeGe sample.
Furthermore, the mean free path of magnons has not been considered in this work. To my knowledge no value of it has been reported in literature for FeGe. For the proposed model it has to be larger than the penetration depth of the microwave.
An argument in favor of the model is the angular dependence of the unidirectional anisotropy. It is typically strongest along the oop-direction, i.e. when the magnetic field points perpendicular to the largest surface of the sample. This is also the orientation in which one would expect the highest unidirectional anisotropy in the proposed model.

6 Discussion and Outlook

This thesis was written with the intention to quantify and eventually explain contributions of DMI in the spin dynamics of cubic FeGe with focus on the dynamic unidirectional anisotropy. The first approach in Sec. 4.1 was to find a phenomenological model to evaluate the strength of the anisotropy. This was done by the introduction of a new term to the free energy density in Eq. 4.1, which is in its simplest form the scalar product of the normalized magnetization with a unidirectional anisotropy field. With this model one is able to fit the measured FMR resonance position and obtain a value for the unidirectional anisotropy constant. This model is a simple tool, which can only be used to quantify the strength and direction of the unidirectional anisotropy. It was not deduced from any interaction or symmetry of the crystal lattice.

The next step was in Sec. 4.2 to check static magnetometry measurements of FeGe along the beforehand determined unidirectional axis for any asymmetry, which could be able to explain the FMR results. The obtained Hysteresis loop was point symmetric, which led to the conclusion, that the unidirectional anisotropy is a dynamic effect only visible during dynamic excitation.

In Sec. 4.3 temperature dependent FMR measurements along the unidirectional axis were performed. Due to a strong distortion of the lineshape at low temperatures a certain feature position in the FMR spectra was chosen and its temperature dependent behavior checked. A change of the feature position after magnetic field inversion is then a measure of the unidirectional anisotropy. So far the unidirectional anisotropy was treated as a difference in the resonance field position. The temperature dependent measurements made it clear, that a temperature difference between both magnetic field directions is also sufficient to explain the experimental results. This temperature difference by itself is temperature dependent as shown in Fig. 4.15 with a maximum of $\Delta T = 7.1\,\mathrm{K} \pm 0.8\,\mathrm{K}$ at $T = 200\,\mathrm{K}$. A temperature model was then applied to the same angular dependent FMR measurement, which was already fitted with the phenomenological model. There a temperature difference of $\Delta T = 3.2\,\mathrm{K} \pm 0.5\,\mathrm{K}$ was determined at $T = 275\,\mathrm{K}$. At this point, similar to the phenomenological model, this temperature difference is only postulated due to its ability to explain the findings.

In Sec. 4.5.1 the FMR lineshape of FeGe was discussed. The linewidth, as shown in Fig. 4.19, follows the same temperature dependent behavior as the magnetization. This led to the conclusion, that the linewidth is driven by an inhomogeneous distribution of demagnetization fields, due to the irregular sample shape and the low penetration depth of the microwaves. The observed resonance line therefore doesn't represent one single state of the sample, but is a distribution of resonance lines of different parts of the sample. The already discussed fit of the resonance line is therefore only valid for the assumption that the point of highest microwave absorption at every angle is related to the same part of the sample. Another key

factor, which could strongly influence the resonance lineshape, is the polycristallinity of the sample. In Sec. 4.5.2 a simulation of the resonance line distribution in a perfect polycrystalline sample of FeGe has been done. The obtained linewidth due to the polycrystallinity was found to be only a minor contribution to the measured FeGe linewidth.
In Ch. 5 the energy was calculated, which is necessary to heat the magnetic system of the sample by the value obtained in Sec. 4.3.1. The calculated energy was below the energy of the injected microwave. Furthermore asymmetric magnon scattering is proposed as an explanation for the dynamic unidirectional anisotropy visible in FeGe. It is based on the non-reciprocity of spin-waves.
Further research is needed to fully understand the unidirectional anisotropy in FeGe. To begin with, the proposed temperature difference has to be checked for its measurability. This can be done with a temperature sensor placed on top of the sample inside an external magnetic field while it is simultaneously excited by microwaves. If no temperature difference between opposite magnetic field directions is detectable, the magnetization has to be measured with the same set-up. A then measured asymmetry in the magnetization would point to an isolated temperature change in the magnetic system. Additionally it is desirable to also check single crystalline FeGe samples for unidirectional anisotropy. Together with the measured dispersion, for example by inelastic neutron scattering, more sophisticated theories can be developed. To reduce the effects of the irregular shape it is reasonable to try to form elliptical shapes of the sample. Then the surface roughness on one side of the sample can be increased gradually to check whether it has a strong influence on the unidirectional anisotropy as suggested in Sec. 5.3.1. A different approach to measure single crystalline FeGe could be the extraction of a single crystallite from the polycrystalline FeGe sample, for example with a focused ion beam, and to then measure FMR in a microresonator. Also FeGe thin films have to be tested for unidirectional anisotropy. Here with ion-implantation gradually more scattering centres could be inserted into the sample to measure its potential influence on the unidirectional anisotropy. Finally, besides FeGe other chiral magnetic systems have to be investigated, from its closest relative MnSi to interfacial DMI samples.

A Appendix

A.1 Ferromagnetic Resonance Spectra of the "Cylindrical" Sample

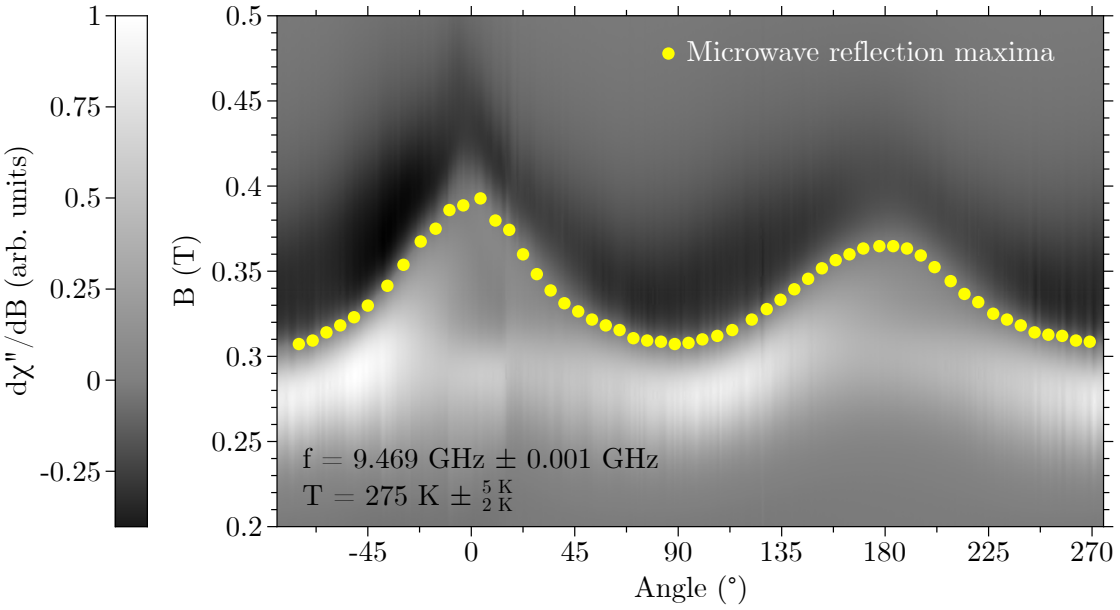

Figure A.1.: Contour plot of the angular dependent FMR spectra of the "cylindrical" FeGe sample. The sample was rotated from ip to oop. 0° denotes oop-direction 1 and 180° oop-direction 2. A unidirectional anisotropy axis is clearly visible along these directions. The frequency was $f = 9.469\,\mathrm{GHz} \pm 0.001\,\mathrm{GHz}$ at a temperature of $T = 275\,\mathrm{K} \pm {}^{5\,\mathrm{K}}_{2\,\mathrm{K}}$. A linear background was subtracted beforehand. The yellow dots indicate the zero crossing of a resonance spectrum, which corresponds to the maximum microwave reflection. For improved clarity only every twelfth maximum is depicted. A time constant of 40.96 ms and a conversion time of 81.92 ms were used together with a microwave power of 1.975 mW. The modulation frequency was 100 kHz with a modulation amplitude of 1×10^{-3} T.

A.2 Dependence of $\tilde{T}$ on the magnetization angles

In Sec. 4.4 a angular dependent temperature $\tilde{T}(\theta, \phi)$ was introduced. It is important to note that its angular dependence is only of static nature. It is not affected by differentiation with respect to θ or ϕ in the determination of the resonance position in Eq. 2.15. This is due to the much slower time scale of this temperature change compared to the dynamic precession of the magnetization. In the same way, these angles are not used in the minimization of the free

energy density to obtain the equilibrium direction of the magnetization. This would cause an additional easy axis along the temperature difference vector, because the magnetization would prefer to point along the direction with the lowest absolute magnetization to minimize the shape anisotropy. Instead an iterative approach is used. In the first step, the free energy density is minimized with respect to θ and ϕ, while $\tilde{T}(\theta, \phi) = \tilde{T}(\theta_B, \phi_B)$. The obtained magnetization angles of this minimization are then θ_1 and ϕ_1. In the next step, the free energy density is again minimized, but for $\tilde{T}(\theta, \phi) = \tilde{T}(\theta_1, \phi_1)$. This is then repeated until self consistency is achieved.

A.3 Modeling of Polycrystals

The purpose of this section is to give a blueprint on how to calculate distributions of resonances based on magnetocrystalline anisotropy and shape anisotropy. Typically, one needs to know such a distribution along a certain direction of the sample shape. In the calculation this direction then aligns with the external magnetic field. Then thousand of resonance fields are calculated for different evenly distributed directions of the magnetocrystalline anisotropy relative to the external magnetic field. This can be implemented into the free energy density in two ways. The first approach is to assume that the magnetic field and the demagnetization tensor are spatially-fixed. Then the magnetocrystalline anisotropy can be rotated in a suitable fashion, resulting in the desired crystalline direction pointing along the external field. The second option is a spatially-fixed magnetocrystalline anisotropy, while the external magnetic field and the demagnetization tensor are rotated. In this work the latter approach was used. To calculated different evenly distributed directions of the magnetocrystalline anisotropy relative to the external magnetic field a method to generate evenly distributed points on a unit sphere is needed. In the following such a method is introduced.

A.3.1 Evenly Distributed Points on a Unitsphere

A lot of programming languages have a command to generate a random number between 0 and 1. Let this random variable be called Z with its realization z. The task is to use this random variable to generate evenly distributed points on the unit sphere. One might think that one only has to randomly generate the spherical angles in the form of $(\Theta_r, \Phi_r) = (\pi z, 2\pi z - \pi)$, which is not the case. The uneven point distribution created by these randomly generated spherical angles can be seen in Fig. A.2. The probability of a certain realization $\theta_r + \mathrm{d}\theta_r$ has to scale with the surface between these angles (with simultaneous integration over all ϕ) in relation to the whole sphere. Due to the special properties of spherical coordinates the surface on a unit sphere scales with the Jacobian determinant $\sin(\theta)$. The Jacobian matrix can therefore be used to calculate the probability density function (PDF) $s_{\Theta_r}(\theta_r)$ to the random variable Θ_r. The PDF is defined in such a way that $s_{\Theta_r}(\theta_r)\,\mathrm{d}\theta_r$ is the probability

to find Θ_r between θ_r and $\theta_r + \mathrm{d}\theta_r$ [95, p. 19]. Since θ_r has to be somewhere between 0 and π to obtain the PDF the Jacobian determinant has to be normalized so that its integral between these limits is 1. The resulting PDF is depicted in Eq. A.1.

$$s_{\Theta_r}(\theta_r) = \frac{\sin(\theta_r)}{2} \tag{A.1}$$

To now calculate the real even distribution of points on the unit sphere one has to apply the inverse transformation method [96, p. 122]. To do that first the cumulative distribution function (CDF) $S_{\Theta_r}(\theta_r)$ has to be calculated through integration of the PDF from 0 to a realization θ_r, which has been done in Eq. A.2. It is the probability, that Θ_r lies somewhere between 0 and θ_r.

$$S_{\Theta_r}(\theta_r) = \int_0^{\theta_r} s_{\Theta_r}(\theta'_r)\,\mathrm{d}\theta'_r = \frac{1-\cos(\theta_r)}{2} \tag{A.2}$$

The inverted CDF as a function of the random variable Z then generates evenly distributed points on the unit sphere. The random variable Θ_r as a function of the random variable Z can is $\Theta_r = S^{-1}_{\Theta_r}(z) = \arccos(1-2z)$. The evenly distributed spherical angles can then be computed through Eq. A.3.

$$(\Theta_r, \Phi_r) = (\arccos(1-2z), 2\pi z - \pi) \tag{A.3}$$

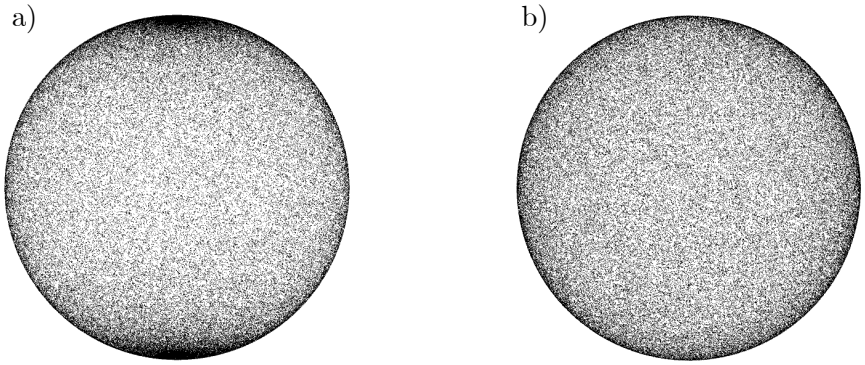

Figure A.2.: a) distribution of points on the unit sphere obtained through $(\Theta_r, \Phi_r) = (\pi z, 2\pi z - \pi)$. The points are not evenly distributed but concentrate on the poles of the sphere, due to a wrong distribution of Θ_r. b) evenly distributed points on the unit sphere obtained through $(\Theta_r, \Phi_r) = (\arccos(1-2z), 2\pi z - \pi)$.

A.3.2 Free Energy Density in Consideration of Rotation Matrices

Now the rotation of the external magnetic field and the demagnetization tensor have to be implemented into the free energy density. We therefore sum up the free energy density terms of the magnetocrystalline ansisotropy (Eq. 3.1), the Zeeman term and the demagnetization term (Eq. 2.6 and Eq. 2.8). However we then have to apply two rotation matrices $\boldsymbol{R}_1$ and $\boldsymbol{R}_2$ to the external magnetic field and the demagnetization tensor respectively in such a way that they are pointing in the direction given by (Θ_r, Φ_r). The thus arising free energy density is written in Eq. A.4.

$$\begin{aligned} F_{\text{rot}} =& K_4(T) \cdot \left(e_{\text{x}}(\theta,\varphi)^2 e_{\text{y}}(\theta,\varphi)^2 + e_{\text{x}}(\theta,\varphi)^2 e_{\text{z}}(\theta,\varphi)^2 + e_{\text{y}}(\theta,\varphi)^2 e_{\text{z}}(\theta,\varphi)^2\right) \\ &+ K_6(T) \cdot \left(e_{\text{x}}(\theta,\varphi)^2 e_{\text{y}}(\theta,\varphi)^2 e_{\text{z}}(\theta,\varphi)^2\right) - \vec{M} \cdot \boldsymbol{R}_1 \cdot \vec{B}_{\text{ext}} \\ &+ \mu_0 \vec{M} \cdot \boldsymbol{R}_2 \cdot \boldsymbol{N} \cdot \boldsymbol{R}_2^{\text{T}} \cdot \vec{M} \end{aligned} \tag{A.4}$$

In the following $\boldsymbol{R}_1$ and $\boldsymbol{R}_2$ are derived. Each rotation has to be around a certain vector $\vec{n}$ by an angle α. The components of an arbitrary rotation matrix $\boldsymbol{R}$ with these properties is shown in Eq. A.5 with the Kroneker delta δ_{ij} and the Levi-Civita symbol ϵ_{ikj}.

$$R_{ij}\left(\vec{t},\alpha\right) = n_i n_j \left(1-\cos(\alpha)\right) + \cos(\alpha)\,\delta_{ij} + \sum_{k=1}^{3} \sin(\alpha)\,\epsilon_{ikj} n_k \tag{A.5}$$

One can presume that the external magnetic field and the demagnetization tensor point in the z-direction of a Cartesian coordinate system before rotation. The vector $\vec{n}$ and the angle α which are necessary to rotate them in a random evenly distributed direction (Θ_r, Φ_r) can then be calculated through Eq. A.6.

$$\begin{aligned} \alpha(\Theta_r) &= \theta_r \\ \vec{n}_r(\Theta_r, \Phi_r) &= \begin{pmatrix} \sin(\theta_r)\cos(\phi_r) \\ \sin(\theta_r)\sin(\phi_r) \\ \cos(\theta_r) \end{pmatrix} \times \begin{pmatrix} 0 \\ 0 \\ 1 \end{pmatrix} \end{aligned} \tag{A.6}$$

A rotation around $\vec{n}_r(\Theta_r, \Phi_r)$ by $\alpha(\Theta_r)$ rotates a vector pointing in the $(0,0,1)$ direction into the direction of $\vec{e}(\Theta_r, \Phi_r)$, which is sufficient for the rotation of the external magnetic field. Therefore $\boldsymbol{R}_1(\Theta_r, \Phi_r) = \boldsymbol{R}(\vec{n}_r(\Theta_r, \Phi_r), \alpha(\Theta_r))$. But one has to be careful when rotating the demagnetization tensor, because it is not explicitly defined, when only a certain direction is given. Due to the occurrence of magnetization directions other than along $\vec{n}_r$ also the "environment" around this direction matters. This is depicted in Fig. A.3 c). To really have a random orientation of the shape anisotropy, one also has to perform a rotation around its own axis, i.e. a random rotation around the $(0,0,1)$ direction in this case, before the actual rotation in the direction of $\vec{e}(\Theta_r, \Phi_r)$ is performed. We therefore introduce another random

azimuth called Φ_a with its realization ϕ_a. The rotation matrix around the $(0,0,1)$ direction is then Eq. A.7.

$$\boldsymbol{R}_a\left(\Phi_r\right) = \begin{pmatrix} \cos\left(\phi_a\right) & -\sin\left(\phi_a\right) & 0 \\ \sin\left(\phi_a\right) & \cos\left(\phi_a\right) & 0 \\ 0 & 0 & 1 \end{pmatrix} \tag{A.7}$$

Due to the associativity of rotation matrices, the rotation matrix acting upon the demagnetization tensor is then the matrix product of $\boldsymbol{R}_1$ and $\boldsymbol{R}_a$, see Eq. A.8.

$$\boldsymbol{R}_2\left(\Theta_r, \Phi_r, \Phi_a\right) = \boldsymbol{R}_1\left(\Theta_r, \Phi_r\right) \cdot \boldsymbol{R}_a\left(\Phi_a\right) \tag{A.8}$$

Now with the right rotation matrices the general method as described in Sec. 4.5.1 and Sec. 4.1 can be used to calculate resonance fields. A histogram of the obtained resonance fields is then the distribution function.

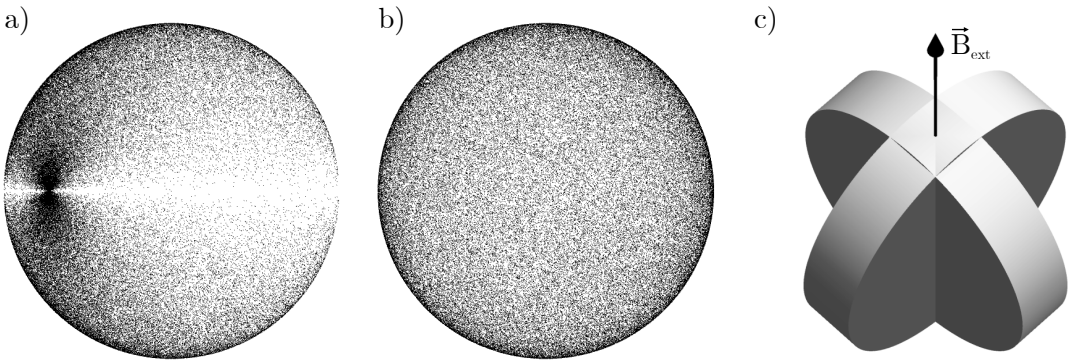

Figure A.3.: a) distribution of the former point $\left(\frac{\pi}{2}, 0\right)$ after $(0,0)$ was rotated to 100,000 randomly distributed points on the unit sphere. An unequal distribution occurs, because no former rotation around the $(0,0)$-axis was applied. b) The same rotation as in a) but with the application of a random rotation around the $(0,0)$-axis. Now the points are randomly distributed as required. c) illustration of the need for an extra random rotation around the $(0,0)$-axis. In a not rotation-symmetric body the surrounding area plays an important role. In this image, two different rotations around the ip-axis of a cylinder are depicted.

References

[1] I. Dzyaloshinsky, "A thermodynamic theory of "weak" ferromagnetism of antiferromagnetics," *Journal of Physics and Chemistry of Solids*, vol. 4, no. 4, pp. 241 – 255, 1958.

[2] T. Moriya, "Anisotropic superexchange interaction and weak ferromagnetism," *Phys. Rev.*, vol. 120, pp. 91–98, 1960.

[3] A. Fert, "Magnetic and transport properties of metallic multilayers," in *Metallic Multilayers*, vol. 59 of *Materials Science Forum*, pp. 439–480, Trans Tech Publications Ltd, 1 1991.

[4] M. Bode, M. Heide, K. Von Bergmann, P. Ferriani, S. Heinze, G. Bihlmayer, A. Kubetzka, O. Pietzsch, S. Blügel, and R. Wiesendanger, "Chiral magnetic order at surfaces driven by inversion asymmetry," *Nature*, vol. 447, no. 7141, p. 190, 2007.

[5] Y. Ishikawa, K. Tajima, D. Bloch, and M. Roth, "Helical spin structure in manganese silicide MnSi," *Solid State Communications*, vol. 19, no. 6, pp. 525–528, 1976.

[6] Y. Ishikawa, G. Shirane, J. A. Tarvin, and M. Kohgi, "Magnetic excitations in the weak itinerant ferromagnet MnSi," *Phys. Rev. B*, vol. 16, pp. 4956–4970, Dec 1977.

[7] P. Bak and M. H. Jensen, "Theory of helical magnetic structures and phase transitions in MnSi and FeGe," *Journal of Physics C: Solid State Physics*, vol. 13, no. 31, pp. L881–L885, 1980.

[8] L. Lundgren, O. Beckman, V. Attia, S. P. Bhattacheriee, and M. Richardson, "Helical spin arrangement in cubic FeGe," *Physica Scripta*, vol. 1, no. 1, pp. 69–72, 1970.

[9] A. N. Bogdanov and U. K. Rößler, "Chiral symmetry breaking in magnetic thin films and multilayers," *Phys. Rev. Lett.*, vol. 87, p. 037203, Jun 2001.

[10] S. Mühlbauer, B. Binz, F. Jonietz, C. Pfleiderer, A. Rosch, A. Neubauer, R. Georgii, and P. Böni, "Skyrmion lattice in a chiral magnet," *Science*, vol. 323, no. 5916, pp. 915–919, 2009.

[11] R. Tomasello, E. Martinez, R. Zivieri, L. Torres, M. Carpentieri, and G. Finocchio, "A strategy for the design of skyrmion racetrack memories," *Scientific reports*, vol. 4, p. 6784, 2014.

[12] X. Zhang, M. Ezawa, and Y. Zhou, "Magnetic skyrmion logic gates: conversion, duplication and merging of skyrmions," *Scientific reports*, vol. 5, p. 9400, 2015.

[13] R. Melcher, "Linear contribution to spatial dispersion in the spin-wave spectrum of ferromagnets," *Physical Review Letters*, vol. 30, no. 4, p. 125, 1973.

[14] J.-H. Moon, S.-M. Seo, K.-J. Lee, K.-W. Kim, J. Ryu, H.-W. Lee, R. D. McMichael, and M. D. Stiles, "Spin-wave propagation in the presence of interfacial dzyaloshinskii-moriya interaction," *Phys. Rev. B*, vol. 88, p. 184404, 2013.

[15] B. W. Zingsem, M. Farle, R. L. Stamps, and R. E. Camley, "Unusual nature of confined modes in a chiral system: Directional transport in standing waves," *Phys. Rev. B*, vol. 99, p. 214429, 2019.

[16] N. Josten, "Dynamische Eigenschaften des chiralen Magneten $Fe_{50}Ge_{50}$ in eingeschränkter Geometrie," Bachelor's thesis, University of Duisburg-Essen, 10 2017.

[17] A. Banholzer, R. Narkowicz, C. Hassel, R. Meckenstock, S. Stienen, O. Posth, D. Suter, M. Farle, and J. Lindner, "Visualization of spin dynamics in single nanosized magnetic elements," *Nanotechnology*, vol. 22, no. 29, p. 295713, 2011.

[18] R. Narkowicz, D. Suter, and R. Stonies, "Planar microresonators for EPR experiments," *Journal of Magnetic Resonance*, vol. 175, no. 2, pp. 275 – 284, 2005.

[19] R. Narkowicz, D. Suter, and I. Niemeyer, "Scaling of sensitivity and efficiency in planar microresonators for electron spin resonance," *Review of Scientific Instruments*, vol. 79, no. 8, p. 084702, 2008.

[20] S. V. Vonsovskii, *Ferromagnetic Resonance, The Phenomenon Of Resonant Absorption Of A High-Frequency Magnetic Field In Ferromagnetic Substances*. Oxford: Pergamon Press Ltd., 1966.

[21] A. G. Gurevich and G. A. Melkov, *Magnetization Oscillations and Waves*. CRC press, 1996.

[22] M. Farle, "Ferromagnetic resonance of ultrathin metallic layers," *Reports on Progress in Physics*, vol. 61, no. 7, pp. 755–826, 1998.

[23] T. Feggeler, "Mikromagnetische simulationen zur statischen und dynamischen charakterisierung von nanopartikeln," Master's thesis, Universität Duisburg-Essen, Germany, 2016.

[24] W. Stoecklein, S. S. P. Parkin, and J. C. Scott, "Ferromagnetic resonance studies of exchange-biased permalloy thin films," *Phys. Rev. B*, vol. 38, pp. 6847–6854, 1988.

[25] H. von Helmholtz, "Die Thermodynamik chemischer Vorgänge," *Sitzungsberichte der Preussischen Akademie der Wissenschaften*, 1882.

[26] H. Flack, "Chiral and achiral crystal structures," *Helvetica Chimica Acta*, vol. 86, no. 4, pp. 905–921, 2003.

[27] M. Richardson, "The partial equilibrium diagram of the Fe-Ge system in the range 40-72 at. % Ge, and the crystallisation of some iron germanides by chemical transport reactions," *Acta Chemica Scandinavica*, vol. 21, no. 21, pp. 2305–2317, 1967.

[28] M. Richardson, "Crystal structure refinements of the B 20 and monoclinic (CoGe-type) polymorphs of FeGe," *Acta Chemica Scandinavica*, vol. 21, no. 21, pp. 753–760, 1967.

[29] A. Aharoni, *Introduction to the Theory of Ferromagnetism*. International Series of Monographs on Physics, Clarendon Press, 2000.

[30] K.-H. Hellwege, *Einführung in die Festkörperphysik*. Berlin: Springer-Verlag, 3rd ed., 1988.

[31] A. I. Akhiezer, V. G. Bar'yakhtar, and M. I. Kaganov, "Reviews of topical problems: Spin waves in ferromagnets and antiferromagnets. I," *Soviet Physics Uspekhi*, vol. 3, pp. 567–592, 1961.

[32] P. Weiss, "L'hypothèse du champ moléculaire et la propriété ferromagnétique," *J. Phys. Theor. Appl.*, vol. 6, no. 1, pp. 661–690, 1907.

[33] W. Heisenberg, "Zur Theorie des Ferromagnetismus," *Zeitschrift für Physik*, vol. 49, pp. 619–636, Sep 1928.

[34] W. Pauli, "Über den Zusammenhang des Abschlusses der Elektronengruppen im Atom mit der Komplexstruktur der Spektren," *Zeitschrift für Physik*, vol. 31, no. 1, pp. 765–783, 1925.

[35] G. Czycholl, *Theoretische Festkörperphysik: von den klassischen Modellen zu modernen Forschungsthemen*. Springer-Verlag, 3 ed., 2007.

[36] J. H. Van Vleck, "On the theory of antiferromagnetism," *The Journal of Chemical Physics*, vol. 9, no. 1, pp. 85–90, 1941.

[37] J. H. Van Vleck and A. Sherman, "The quantum theory of valence," *Rev. Mod. Phys.*, vol. 7, pp. 167–228, 1935.

[38] P. Zeeman, "On the influence of magnetism on the nature of the light emitted by a substance," *The London, Edinburgh, and Dublin Philosophical Magazine and Journal of Science*, vol. 43, no. 262, pp. 226–239, 1897.

[39] R. I. Joseph and E. Schlömann, "Demagnetizing field in nonellipsoidal bodies," *Journal of Applied Physics*, vol. 36, no. 5, pp. 1579–1593, 1965.

[40] A. Vansteenkiste, J. Leliaert, M. Dvornik, M. Helsen, F. Garcia-Sanchez, and B. Van Waeyenberge, "The design and verification of mumax3," *AIP Advances*, vol. 4, no. 10, p. 107133, 2014.

[41] M. Beleggia, M. D. Graef, and Y. T. Millev, "The equivalent ellipsoid of a magnetized body," *Journal of Physics D: Applied Physics*, vol. 39, no. 5, p. 891, 2006.

[42] L. Landau and E. Lifshitz, "Anomalous high-frequency resistance of ferromagnetic metals," *Phys. Z. Sowjetunion*, vol. 8, p. 153–169, 1935.

[43] T. L. Gilbert, "A phenomenological theory of damping in ferromagnetic materials," *IEEE Transactions on Magnetics*, vol. 40, no. 6, pp. 3443–3449, 2004.

[44] B. W. Zingsem, M. Winklhofer, R. Meckenstock, and M. Farle, "Unified description of collective magnetic excitations," *Phys. Rev. B*, vol. 96, p. 224407, 2017.

[45] J. C. Slater, "Microwave electronics," *Rev. Mod. Phys.*, vol. 18, pp. 441–512, 1946.

[46] R. Meckenstock, "Invited review article: Microwave spectroscopy based on scanning thermal microscopy: Resolution in the nanometer range," *Review of Scientific Instruments*, vol. 79, no. 4, p. 041101, 2008.

[47] B. W. Zingsem, "A theory of the magnetodynamic response function," Master's thesis, Universität Duisburg-Essen, Germany, 2016.

[48] F. J. Dyson, "Electron spin resonance absorption in metals. II. theory of electron diffusion and the skin effect," *Phys. Rev.*, vol. 98, pp. 349–359, 1955.

[49] H. Suhl, "Ferromagnetic resonance in nickel ferrite between one and two kilomegacycles," *Phys. Rev.*, vol. 97, pp. 555–557, 1955.

[50] E. Schlömann and J. R. Zeender, "Ferromagnetic resonance in polycrystalline nickel ferrite aluminate," *Journal of Applied Physics*, vol. 29, no. 3, pp. 341–343, 1958.

[51] E. Schlömann and R. V. Jones, "Ferromagnetic resonance in polycrystalline ferrites with hexagonal crystal structure," *Journal of Applied Physics*, vol. 30, no. 4, pp. S177–S178, 1959.

[52] W. T. Lord Kelvin, *Baltimore lectures on molecular dynamics and the wave theory of light*. Cambridge: C. J. Clay and sons, 1904.

[53] G. Fasman, *Circular Dichroism and the Conformational Analysis of Biomolecules*. Siberian School of Algebra and Logic, Springer US, 1996.

[54] A. Ullah, B. Balamurugan, W. Zhang, S. Valloppilly, X. . Li, R. Pahari, L. . Yue, A. Sokolov, D. J. Sellmyer, and R. Skomski, "Crystal structure and Dzyaloshinski–Moriya micromagnetics," *IEEE Transactions on Magnetics*, vol. 55, pp. 1–5, July 2019.

[55] V. Dmitriev, D. Chernyshov, S. Grigoriev, and V. Dyadkin, "A chiral link between structure and magnetism in MnSi," *Journal of Physics: Condensed Matter*, vol. 24, p. 366005, aug 2012.

[56] S.-A. Siegfried, *Chirality effects in transition metal monogermanides and -silicides*. PhD thesis, University of Hamburg, 2016.

[57] R. Wyckoff, *The Analytical Expression of the Results of the Theory of Space-groups*. Carnegie Institution of Washington publication, Carnegie Institution of Washington, 1922.

[58] L. Lundgren, K. Blom, and O. Beckman, "Magnetic susceptibility measurements on cubic FeGe," *Physics Letters A*, vol. 28, no. 3, pp. 175 – 176, 1968.

[59] R. Wäppling and L. Häggström, "Mössbauer study of cubic FeGe," *Physics Letters A*, vol. 28, no. 3, pp. 173 – 174, 1968.

[60] R. Wäppling, L. Häggström, and E. Karlsson, "Magnetic properties of FeGe studied by Mössbauer effect," *Physica Scripta*, vol. 2, no. 4-5, pp. 233–236, 1970.

[61] H. Wilhelm, M. Baenitz, M. Schmidt, U. K. Rößler, A. A. Leonov, and A. N. Bogdanov, "Precursor phenomena at the magnetic ordering of the cubic helimagnet FeGe," *Phys. Rev. Lett.*, vol. 107, p. 127203, Sep 2011.

[62] L. Xu, H. Han, J. Fan, D. Shi, D. Hu, H. Du, L. Zhang, Y. Zhang, and H. Yang, "Magnetic entropy change and accurate determination of Curie temperature in single-crystalline helimagnet FeGe," *EPL (Europhysics Letters)*, vol. 117, no. 4, p. 47004, 2017.

[63] T. Komatsubara, S. Kusaka, and Y. Ishikawa, "Proc. 6th int. conf. internal friction and ultrasonic attenuation in solids," *University of Tokyo Press*, p. 237, 1977.

[64] K. Kadowaki, K. Okuda, and M. Date, "Magnetization and magnetoresistance of MnSi. I," *Journal of the Physical Society of Japan*, vol. 51, no. 8, pp. 2433–2438, 1982.

[65] S. V. Grigoriev, S. V. Maleyev, A. I. Okorokov, Y. O. Chetverikov, and H. Eckerlebe, "Field-induced reorientation of the spin helix in MnSi near T_c," *Phys. Rev. B*, vol. 73, p. 224440, 2006.

[66] C. Thessieu, C. Pfleiderer, A. N. Stepanov, and J. Flouquet, "Field dependence of the magnetic quantum phase transition in MnSi," *Journal of Physics: Condensed Matter*, vol. 9, no. 31, pp. 6677–6687, 1997.

[67] W. Münzer, A. Neubauer, T. Adams, S. Mühlbauer, C. Franz, F. Jonietz, R. Georgii, P. Böni, B. Pedersen, M. Schmidt, A. Rosch, and C. Pfleiderer, "Skyrmion lattice in the doped semiconductor $Fe_{1-x}Co_xSi$," *Phys. Rev. B*, vol. 81, p. 041203, Jan 2010.

[68] C. Pfleiderer, T. Adams, A. Bauer, W. Biberacher, B. Binz, F. Birkelbach, P. Böni, C. Franz, R. Georgii, M. Janoschek, F. Jonietz, T. Keller, R. Ritz, S. Mühlbauer, W. Münzer, A. Neubauer, B. Pedersen, and A. Rosch, "Skyrmion lattices in metallic and semiconducting B20 transition metal compounds," *Journal of Physics: Condensed Matter*, vol. 22, no. 16, p. 164207, 2010.

[69] H. Wilhelm, M. Baenitz, M. Schmidt, C. Naylor, R. Lortz, U. K. Rößler, A. A. Leonov, and A. N. Bogdanov, "Confinement of chiral magnetic modulations in the precursor region of FeGe," *Journal of Physics: Condensed Matter*, vol. 24, p. 294204, jul 2012.

[70] S. Haraldson, L. Björn, O. Beckman, and U. Smith, "Magnetic resonance in cubic FeGe," *Journal of Magnetic Resonance*, vol. 8, no. 3, pp. 271–273, 1972.

[71] S. Haraldson and U. Smith, "The microwave resonance line shape in ferromagnetic cubic FeGe," *Journal of Physics and Chemistry of Solids*, vol. 35, no. 9, pp. 1237–1245, 1974.

[72] U. Smith and S. Haraldson, "Spin-wave resonances in cubic FeGe," *Journal of Magnetic Resonance (1969)*, vol. 16, no. 3, pp. 390–401, 1974.

[73] S. Haraldson, L. Pettersson, and S. Bhagat, "Frequency and temperature dependence of spin resonances in cubic FeGe," *Journal of Magnetic Resonance*, vol. 32, no. 1, pp. 115 – 120, 1978.

[74] S. Grytsiuk, M. Hoffmann, J.-P. Hanke, P. Mavropoulos, Y. Mokrousov, G. Bihlmayer, and S. Blügel, "Ab initio analysis of magnetic properties of the prototype B20 chiral magnet FeGe," *Physical Review B*, vol. 100, no. 21, p. 214406, 2019.

[75] E. Turgut, H. Paik, K. Nguyen, D. A. Muller, D. G. Schlom, and G. D. Fuchs, "Engineering Dzyaloshinskii-Moriya interaction in B20 thin-film chiral magnets," *Physical Review Materials*, vol. 2, no. 7, p. 074404, 2018.

[76] M. Beg, M. Albert, M.-A. Bisotti, D. Cortés-Ortuño, W. Wang, R. Carey, M. Vousden, O. Hovorka, C. Ciccarelli, C. S. Spencer, C. H. Marrows, and H. Fangohr, "Dynamics of skyrmionic states in confined helimagnetic nanostructures," *Phys. Rev. B*, vol. 95, p. 014433, 2017.

[77] S. Zhang, I. Stasinopoulos, T. Lancaster, F. Xiao, A. Bauer, F. Rucker, A. Baker, A. Figueroa, Z. Salman, F. Pratt, *et al.*, "Room-temperature helimagnetism in FeGe thin films," *Scientific reports*, vol. 7, no. 1, p. 123, 2017.

[78] E. Turgut, A. Park, K. Nguyen, A. Moehle, D. A. Muller, and G. D. Fuchs, "Chiral magnetic excitations in FeGe films," *Phys. Rev. B*, vol. 95, p. 134416, 2017.

[79] E. Turgut, M. J. Stolt, S. Jin, and G. D. Fuchs, "Topological spin dynamics in cubic FeGe near room temperature," *Journal of Applied Physics*, vol. 122, no. 18, p. 183902, 2017.

[80] N. Kawai and S. Endo, "The generation of ultrahigh hydrostatic pressures by a split sphere apparatus," *Review of Scientific Instruments*, vol. 41, no. 8, pp. 1178–1181, 1970.

[81] D. Walker, M. A. Carpenter, and C. M. Hitch, "Some simplifications to multianvil devices for high pressure experiments," *American Mineralogist*, vol. 75, no. 9-10, p. 1020, 1990.

[82] W. H. Bragg and W. L. Bragg, "The reflection of X-rays by crystals," *Proceedings of the Royal Society of London. Series A, Containing Papers of a Mathematical and Physical Character*, vol. 88, no. 605, pp. 428–438, 1913.

[83] W. H. Miller, *A treatise on crystallography*. For J. & JJ Deighton, 1839.

[84] B. Fultz and J. M. Howe, *Transmission Electrion Microscopy and Diffractometry of Materials*. Springer Science & Business Media, 3 ed., 2008.

[85] J. Brentano, "Focussing method of crystal powder analysis by X-rays," *Proceedings of the Physical Society of London*, vol. 37, no. 1, p. 184, 1924.

[86] P. Scherrer, "Bestimmung der inneren Struktur und der Größe von Kolloidteilchen mittels Röntgenstrahlen," in *Kolloidchemie Ein Lehrbuch*, pp. 387–409, Springer, 1912.

[87] S. Foner, "Versatile and sensitive vibrating-sample magnetometer," *Review of Scientific Instruments*, vol. 30, no. 7, pp. 548–557, 1959.

[88] P. David and M. Heath, "Further comments on the shape dependent demagnetizing field in ferromagnetic resonance," *Journal of Physics C: Solid State Physics*, vol. 4, no. 13, p. L282, 1971.

[89] M. Farle, *Magnetische Resonanz an Gd(0001) Monolagen auf W(110) in der Nähe der Curietemperatur*. PhD thesis, Freie Universität Berlin, 1989.

[90] J. V. Vleck, "Ferromagnetic resonance," *Physica*, vol. 17, no. 3, pp. 234 – 252, 1951.

[91] D. Stancil and A. Prabhakar, *Spin Waves: Theory and Applications*. Springer US, 2009.

[92] C. Kittel, *Quantum theory of solids*. New York: Wiley, 1963.

[93] W. Demtröder, *Experimentalphysik*. Springer, 8 ed., 2018.

[94] S. Rezende, R. Rodríguez-Suárez, J. L. Ortiz, and A. Azevedo, "Thermal properties of magnons and the spin seebeck effect in yttrium iron garnet/normal metal hybrid structures," *Physical Review B*, vol. 89, no. 13, p. 134406, 2014.

[95] T. Fließbach, *Statistische Physik*. Springer, 5 ed., 2010.

[96] H. Tanizaki, *Computational methods in statistics and econometrics*. CRC Press, 2004.

Danksagung

Ich danke Herrn Prof. Dr. Michael Farle für die Möglichkeit meine Arbeit in seiner Arbeitsgruppe anzufertigen und dass ich stets meine eigenen Ideen und Ansätze verfolgen durfte. Trotzdem hatte er immer ein offenes Ohr und Intresse an meiner Arbeit.

Ich bin auch Herrn Benjamin Zingsem zu Dank verpflichtet, der mich von Anfang an unterstützt und bei jeder Phase dieser Arbeit begleitet, beraten und mir geholfen hat.

Ich danke Dr. Ralf Meckenstock für seine ständige Hilfsbereitschaft. Seine Tür stand für Fragen immer offen.

Ich danke Dr. Detlef Spoddig für seine Hilfe bei jeglichen technischen Problemen und insbesondere für seine Hilfe bei den K-Band FMR Messungen.

Ich bedanke mich bei Dr. Marina Spasova für die Magnetometrie Messungen von FeGe.

Ich möchte Prof. i.R. Dr. Mehmet Acet für seine Hilfe bei den XRD Messungen danken.

Ich danke Dr. Iliya Radulov aus der Arbeitsgruppe von Prof. Dr. Oliver Gutfleisch für die Synthese der FeGe Proben.

Ich danke Thomas Feggeler für sein Vertrauen bei der Übergabe des FeGe Projekts an mich und seine immerwährende Hilfsbereitschaft.

Ich möchte Paul Wendtland für seine Hilfe beim Löten des Temperatursensors und bei den Mikroskopbildern der Probe danken.

Weiterhin danke ich Michael Vennemann, Philipp Kükenbrink und Daniel Scholz, die mir bei technischen Problemen und Aufgaben zur Seite standen.

Ich bedanke mich bei Sabina Grubba und Helga Mundt für die ausgezeichnete Teamassistenz

Ich danke der gesamten Arbeitsgruppe für eine tolle Arbeitsatmosphäre und anregende Gespräche und Diskussionen.

Ich danke Nico Hahn, Jakob Penner und Henning Rudolph für ihre langjährige Freundschaft und ihre Unterstützung beim gemeinsamen Physikstudium.

Mein besonderer Dank gilt Sandra Krach, die mir über die gesamte Masterarbeit hinweg in jeder Lebenslage zur Seite stand.

Selbstständigkeitserklärung

Ich, Nicolas Josten, versichere hiermit, dass ich diese Masterarbeit mit dem Titel „Dynamic Unidirectional Anisotropy in FeGe studied by Ferromagnetic Resonance“ selbstständig verfasst und keine anderen als die angegebenen Quellen und Hilfsmittel benutzt habe.

Ort, Datum

Unterschrift